Working together to control mutation: how collective peroxide detoxification determines microbial mutation rate plasticity.

Rowan Green[1], Hejie Wang[2], Carol Botchey[2], Nancy Zhang[2], Charles Wadsworth[2], Andrew J McBain[3], Pawel Paszek[2,4], Rok Krašovec[2]†, Christopher G Knight[1]†

1. School of Natural Sciences, Faculty of Science & Engineering, University of Manchester
2. School of Biological Sciences, Faculty of Biology, Medicine & Health, University of Manchester
3. School of Health Sciences, Faculty of Biology Medicine & Health, University of Manchester
4. Institute of Fundamental Technological Research, Polish Academy of Sciences, Warsaw, Poland
† Corresponding Author

Email: chris.knight@manchester.ac.uk (CGK); rok.krasovec@manchester.ac.uk (RK)

Abstract

Mutagenesis is responsive to many environmental factors. Evolution therefore depends on the environment not only for selection but also in determining the variation available in a population. One such environmental dependency is the inverse relationship between mutation rates and population density in many microbial species. Here we determine the mechanism responsible for this mutation rate plasticity. Using dynamical computational modelling and *in vivo* mutation rate estimation we show that the negative relationship between mutation rate and population density arises from the collective ability of microbial populations to control concentrations of hydrogen peroxide. We demonstrate a loss of this density-associated mutation rate plasticity when *Escherichia coli* populations are deficient in the degradation of hydrogen peroxide. We further show that the reduction in mutation rate in denser populations is restored in peroxide degradation-deficient cells by the presence of wild-type cells in a mixed population. Together, these model-guided experiments provide a mechanistic explanation for density-associated mutation rate plasticity, applicable across all domains of life, and frames mutation rate as a dynamic trait shaped by microbial community composition.

Introduction

Uncovering the mechanisms behind environmentally responsive mutagenesis informs our understanding of evolution, notably antimicrobial resistance, where mutation supply can be critical (1, 2). Microbial mutation rates are responsive to a wide variety of environmental factors including population density (3), temperature (4), growth rate (5, 6), stress (7, 8), growth phase (9) and nutritional state (10). Such mutation rate plasticity inspires the idea of "anti-evolution drugs", able to slow the evolution of antimicrobial resistance during the treatment of an infection (2, 11-13). Even small reductions in the mutation rate (2-5-fold) can have dramatic effects on the capacity of bacterial populations to adapt to antibiotic treatment, particularly when evolution is limited by mutation supply, as is the case for small pathogen populations (2).

Microbial mutation rates have an inverse association with population density across all domains of life, we have previously shown that 93% of otherwise unexplained variation in published mutation rate estimates is explained by the final population density (3). This density-associated mutation rate plasticity (DAMP) is a distinct phenotype from stress-induced mutagenesis, which acts via independent genetic mechanisms (14). Population density alters not only the rate but also the spectrum of mutations, with significantly higher rates of AT>GC transitions seen in low density populations (15). Density effects are likely relevant to natural populations given that population sizes and densities vary greatly, for example, *Escherichia coli* populations in host faeces can range in density by 5 orders of magnitude (16), and infections can be established by populations as small as $6x10^3$ cells (17). We therefore aim to mechanistically describe the widespread phenotype of DAMP.

In order to test potential mechanisms generating DAMP, we developed and systematically assessed a computational model connecting metabolism and mutagenesis in a growing *E. coli* population. This model generates the hypothesis that the key determinants of DAMP are the production and degradation rates of reactive oxygen species (ROS). Though molecular oxygen is relatively stable it can be reduced to superoxide ($^{\bullet}O_2^-$), hydrogen peroxide (H_2O_2) and hydroxyl radicals ($HO^{\bullet}$). These "reactive oxygen species" are strong oxidants able to damage multiple biological molecules including nucleotides and DNA (18). We tested the role of ROS in controlling DAMP by estimating mutation rate plasticity under different conditions of environmental oxygen and with genetic manipulations known to alter ROS dynamics. We find that the reduction in

mutation rate at increased population density results from the population's increased ability to degrade H_2O_2, resulting in reduced ROS-associated mutagenesis. We show that this density effect is also experienced by cells deficient in H_2O_2 degradation when cocultured with wild-type cells able to detoxify the environment. Mutation rates therefore depend not only on the genotype of the individual but also on the community's capacity to degrade H_2O_2.

Results

Initial computational model of nucleotide metabolism in a growing microbial population fails to reproduce mutation rate plasticity

To generate hypotheses for the mechanisms of density-associated mutation rate plasticity we constructed a system of ordinary differential equations (ODEs) that recapitulates the dynamics of metabolism, growth and mutagenesis in a 1mL batch culture of *E. coli* (Fig. 1). The enzyme MutT, responsible for degrading mutagenic oxidised GTP (19), is essential in DAMP (3); the ODE model is therefore focussed on guanine bases. In the model external glucose (***eGlc***) is taken up by a small initial *E. coli* population (***wtCell***). Internal glucose (***iGlc***) is then metabolised to produce ***ROS***, ***dGTP*** and, largely, 'other' molecules ('Sink' in Fig. 1). ***dGTP*** is then either integrated into a newly synthesised DNA molecule (***DNA***) or it reacts with ***ROS*** to produce 8-oxo-2'-deoxyguanosine triphosphate (***odGTP***). In this model, non-oxidised ***dGTP*** always pairs correctly with cytosine, producing non-mutant DNA (***DNA***). In a second round of DNA replication the guanine base is now on the template strand, cytosine is correctly inserted opposite producing new chromosomes (***wtCell***). ***odGTP***, if it is not dephosphorylated by MutT into *dGMP* (Sink), can either pair correctly with cytosine (becoming ***DNA***) or mis-pair with adenine (becoming ***mDNA***). When ***odGTP*** is inserted opposite adenine into DNA (***mDNA***) it may be repaired by the MutS or MutY proteins, converting the ***mDNA*** back to ***DNA***. The key output of interest is the mutation rate, which is defined as the number of mutant base pairs (***mCell***) divided by the number of non-mutant base pairs (***wtCell***). The model comprises 10 ordinary differential equations (ODEs), one for each substance variable in Fig.1 (excluding 'Sink'), plus ***cytVol***, the total population cytoplasmic volume within which all the reactions occur (Table 1, Eq. 1-10, Methods). These equations require 14 parameters (some of them composite, Table 2); the structure and parameter values are largely taken from the existing literature (for details see Methods). Un-measurable parameters (notably the rate of ***dGTP*** oxidation to ***odGTP*** by ***ROS***, '**O2'**) were set to give the observed mutation rate (2×10^{-10} mutations per base pair per generation, (20)) at a final population density of 3×10^8 CFU ml^{-1}, typical of 250 mg L^{-1} glucose in minimal media. As with most experiments demonstrating density-associated mutation rate plasticity (3, 21), final population density is controlled by varying initial external glucose. We initiated 28h simulations of 1ml cultures with 2175 cells (a small number, typical of fluctuation assays estimating mutation rate, Fig. S10), no internal metabolites and external glucose concentrations relevant to wet-lab experiments – across a log scale from 55 to 1100 mg L^{-1} (Table 1). The dynamics of external glucose, population size and mutation rate for these simulations are shown in Fig.1B-D.

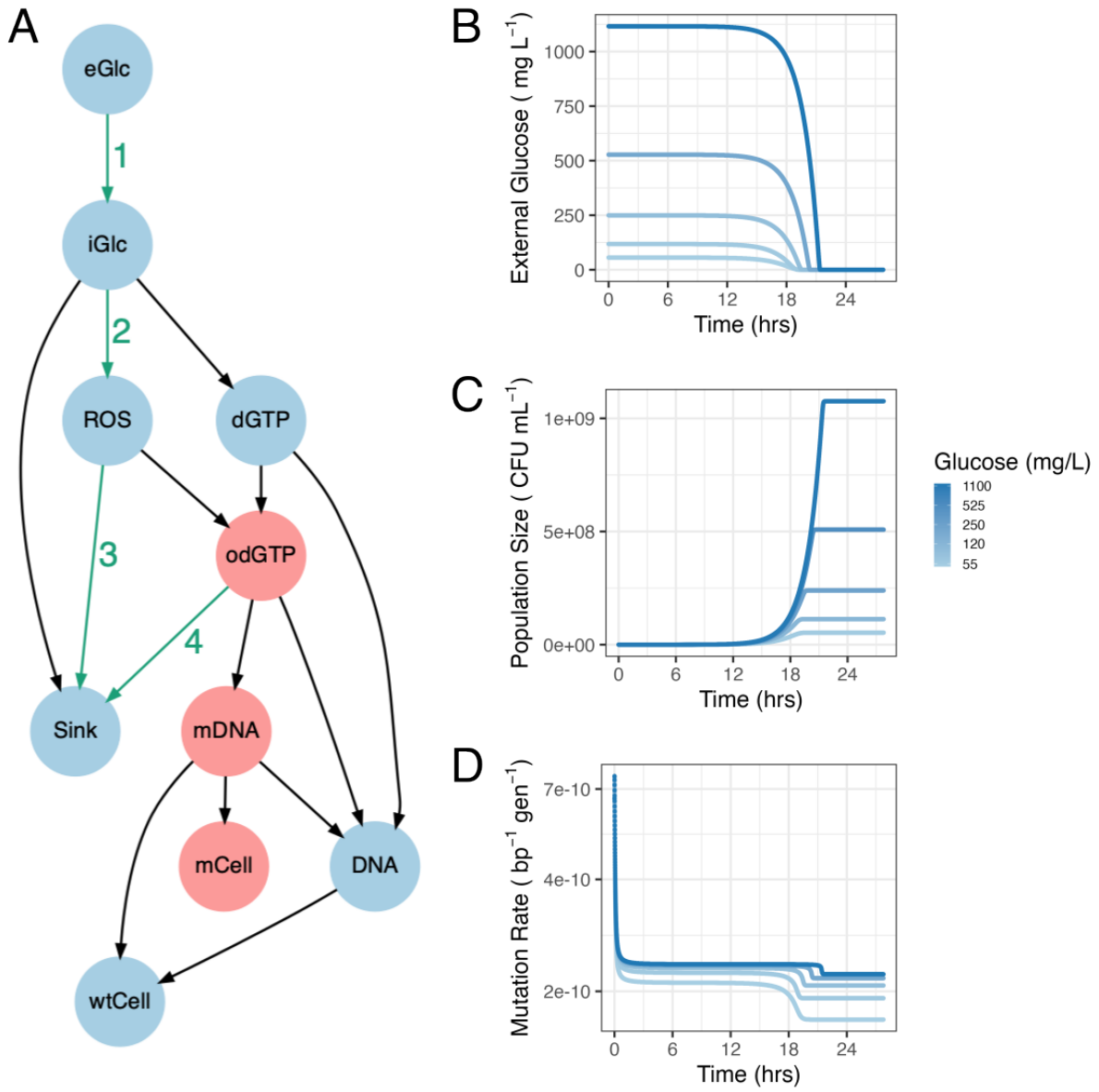

Figure 1: Dynamical computational model of growth, metabolism and mutagenesis in E. coli*. A: Model structure connecting variables. Red variables indicate the pathway to mutagenesis; green numbered arrows indicate pathways targeted by model variants. This structure was represented in ODEs, parameterised from the literature (Methods), and simulated to give output shown in B-D. B: Kinetics of external glucose concentration (eGlc), C: population size (wtCell divided by G nucleotides in the E. coli genome) and D: mutation rate (mCell/wtCell). Note log scale on y-axis in panel D. Panels B-D are plotted for 5 initial glucose concentrations (range 55 – 1100 mg L^{-1} as shown in legend), initial glucose concentration indicated by line colour.*

This initial model (Fig 1, referred to as model A) creates an approximately linear log-log slope of 0.09 ± 0.06 (95% CI) between final population and mutation rate (Red line, Fig.2A, Regression 1 (SI)). We can compare the slope directly to *in vivo* estimates of mutation rates in *E. coli*, which show strong DAMP, with a slope of -0.84 ± 0.13 (95% CI, grey dots and dashed line, Fig. 2A, Regression 2 (SI)). Model A is therefore not describing the processes causing DAMP – the structure and/or the parameters used are either incomplete or fail to replicate biology for some other reason. To test whether inappropriate parameter values could be responsible for the lack of DAMP in model A, we simulated 50,000 parameter sets simultaneously varying all parameters randomly across 10% – 1,000% of their original value. These results were filtered as described in Methods and are plotted in

Fig. 2B. This global sensitivity analysis showed the mutation rate plasticity, i.e., slope of model A to be very robust, with an interquartile range of 0.02-0.13 as shown by error bars in Fig.2B. All tested parameter sets gave a log-log linear slope of > - 0.05, suggesting that DAMP requires processes not represented in this initial model.

ROS production and degradation are central to density-associated mutation rate (DAMP) plasticity *in silico*

While there was only limited variation in the relationship between mutation rate and population density, defining the slope of DAMP, in model A (Fig. 2B) we can ask which model parameters are associated either with this variation or with variation in mutation rate itself (Fig. S1). The affinity of importers for glucose (Ks, part of reaction 1 in Fig. 1A) had by far the closest association with the slope (Spearman's Rho $_{(DF = 3583)}$ = 0.91, $P < 2.2 \times 10^{-16}$, Fig. S1), whereas a group of parameters, including parameters controlling the rates of both ***ROS*** production (r, reaction 2 in Fig. 1A) and ***ROS*** degradation (parameters O2 and O3, corresponding to reaction 3 in Fig. 1A) had the closest association with the mutation rate (Spearman's Rho $_{(DF = 3583)}$ = 0.22, 0.21 and -0.21 respectively, all $P < 2.2 \times 10^{-16}$ Fig. S1). The parameter representing MutT activity (parameter C1, reaction 4, Fig. 1A), found to be relevant in previous work on DAMP (3), was also in this group of parameters controlling mutation rate and so was also considered as candidate processes for further exploration. We hypothesise that the additional processes required to reproduce DAMP as observed in the lab are associated with these reactions (numbered 1-4 in Fig. 1A). We systematically tested each of these processes using structural variants to the model, explicitly modifying density dependence in biologically plausible ways. We thus use these models as a method of hypothesis generation, to determine which mechanisms may plausibly cause DAMP, with a view to testing these candidate mechanisms in the lab.

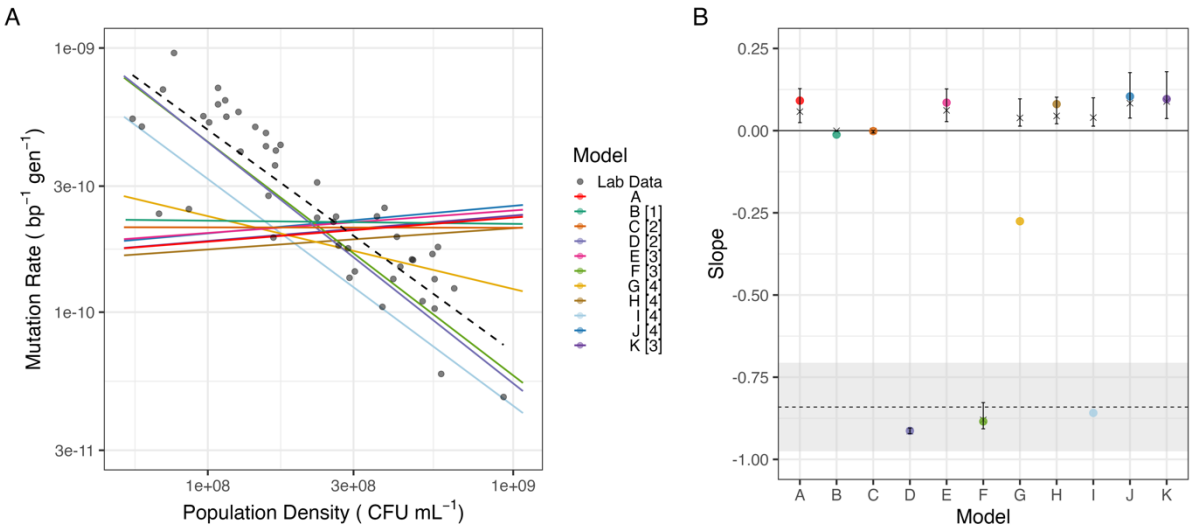

Figure 2: Mutation rates in model variants*. A) Solid coloured lines show fitted log-log linear relationship between final population density and mutation rate for models A to K (Regression 1 (SI)); numbers [1] – [4] in legend indicate the pathway targeted from Fig. 1A. Black points and dashed line show lab data for E. coli wild-type BW25113 in glucose minimal media with a log-log linear regression fitted (Regression 2 (SI)). B) Global sensitivity analysis; coloured points show slopes from baseline parameters (as in 2A), and crosses and error bars show median and interquartile range of slope across 5x10^5 randomly perturbed parameter sets, models are coloured as in Fig. 2A. Dashed line shows slope of lab data in Fig. 2A (Regression 2), and grey area shows 95% CI on this slope.*

The slight increase in mutation rates seen as density increases in model A (a reversal of the negative association seen in the DAMP phenotype, therefore referred to as 'reverse DAMP') is the

result of increased external glucose leading to increased internal glucose concentrations (Fig. S2), creating an increased rate of ***ROS*** production and therefore higher mutation rates. It is therefore plausible that if glucose importer proteins are more expressed under low external glucose conditions, increasing the rate of reaction 1 (Fig. 1A) at low glucose concentrations may increase mutation rates at low density. Introducing this model variant (model B, using Eq. 1_B) does indeed remove model A's positive association between mutation rate and density but does not give the negative association observed *in vivo* (model B slope = -0.01 ± 0.06 (95% CI), Fig. 2, Regression 1 (SI)).

In model A, ***ROS*** are produced only by cellular metabolism, however lab media also accumulates significant concentrations of H_2O_2 through photochemistry (22). This is represented in model C by replacing reaction 2 (Fig. 1A) with a constant ***ROS*** concentration in the system (using Eq. 8_C rather than Eq. 8) and in model D by a constant rate of ***ROS*** production (using Eq. 7_D rather than Eq. 7). Both models abolish model A's positive slope. However, while model C removes DAMP (slope = -0.001 ± 0.06 (95% CI), Regression 1 (SI)), model D introduces a strong negative slope similar to the laboratory data (slope = -0.91 ± 0.06 (95% CI), Regression 1 (SI)).

Decreasing mutation rates at higher population densities could also be the result of changes in cellular ROS degradation rates (reaction 3). We therefore created models where degradation is determined by the internal glucose concentration (model E) and by the population density (model F), replacing Eq. 7 with Eq. 7_E and 7_F respectively. Of these two, the first had very little effect (model E, slope = 0.09 ± 0.06 (95% CI), Regression 1 (SI)) whereas the second had a large effect, giving a strong slope similar to the laboratory data (model F, slope = -0.89 ± 0.06 (95% CI), Regression 1 (SI)).

Given that previous work has shown the action of MutT in degrading ROS-damaged dGTP (***odGTP***, Fig. 1A) to be essential to DAMP (3), we explored models in which the rate of ***odGTP*** degradation by MutT (reaction 4, Fig. 1A) is determined by the internal glucose (model G, using Eq. 8_G rather than Eq. 8), ***odGTP*** (model H, using Eq. 8_H rather than Eq. 8) or ***ROS*** concentration (model I, using Eq. 8_I rather than Eq. 8). None of these models consistently resulted in DAMP (Fig. 2B): making MutT activity dependent on ***odGTP*** had very little effect at all (model H, slope = 0.08 ± 0.06 (95% CI), Regression 1 (SI)) whereas making MutT activity directly responsive to internal glucose or ROS concentration did reproduce some degree of DAMP slope (models G and I slopes -0.28 ± 0.06 and -0.86 ± 0.06 respectively (95% CI), Regression 1 (SI)). However, the DAMP slopes of models G and I are highly parameter dependent with the majority of parameter combinations in the global sensitivity analysis giving very little slope at all (Fig. 2B).

Finally, we replaced model A's mass action dynamics with saturating Michaelis Menten kinetics for MutT activity (reaction 4, model J using Eq. 7_J rather than Eq. 7 (19)) and enzymatic degradation of H_2O_2 (reaction 3, model K using Eq.7_{KA} and Eq.7_{KB} rather than Eq. 7, (23)). Neither of these modifications greatly affected the mutation rate response of the model to population density (slope = 0.104 ± 0.06 and 0.096 ± 0.06 respectively, (95% CI), Regression 1 (SI), Fig. 2). Thus, across 11 biologically plausible model structures only two, D and F, affecting reactions 2 and 3 respectively in specific ways, produced DAMP comparable to that observed in the laboratory (Fig. 2A) and robust to parameter variations (Fig. 2B).

We can use these model findings for hypothesis generation: Model A (without DAMP) only describes ROS production from metabolism, whereas Model D (with DAMP) modifies the initial model to have a constant rate of ROS generation, independent of the cell density. Model D is consistent with ROS production in the system being dominated by environmental sources at a constant rate. If DAMP is a result of such environmental ROS production, we would expect this phenotype to be absent under anaerobic conditions where external H_2O_2 production is negligible (22).

Model F, which gains DAMP relative to model A, describes an increased rate of ROS detoxification dependent on the population density. This reflects a system in which ROS detoxification is primarily occurring within cells. Here ROS diffusion into cells from the environment is significant and therefore the environment is more efficiently detoxified by larger populations. If DAMP is a result of an increased environmental detoxification capacity in dense populations in this way, we expect strains deficient in ROS degradation not to show DAMP. We would further expect dense populations to show greater removal of environmental ROS than low-density populations.

We therefore go on to test these predictions *in vivo* using fluctuation assays to estimate the mutation rate in batch cultures of *E. coli.*

Environmental oxygen is necessary for DAMP *in vivo*

To test the hypothesis (from model D) that DAMP is dependent on external oxygen (from model D) we estimated mutation rates of *E. coli* under anaerobiosis across a range of nutrient-determined final population densities, analysing the results using a linear mixed effects model (Regression 4 (SI)). We find that anaerobic growth results in a loss of the negative relationship between density and mutation rate, indeed mutation rates significantly increased with density (slope = 0.6 ± 0.42 (95% CI), Fig. 3B, statistical tests in Table S1, Regression 4 (SI)). We further test this relationship using a second wild-type strain (*E. coli* MG1655). Again, we see a loss of DAMP under anaerobiosis (slope = 0.12 ± 0.7 (95% CI), cf. slope = -0.43 ± 0.25 (95%CI), anaerobic and aerobic respectively, Regression 4 (SI), Fig. S3). This supports the hypothesis arising from model D that, when external ROS production is substantial (model D / aerobiosis) mutation rates fall with increasing final population size, whilst when external ROS production is not included (model A / anaerobiosis) mutation rates remain similar or increase slightly with higher cell densities.

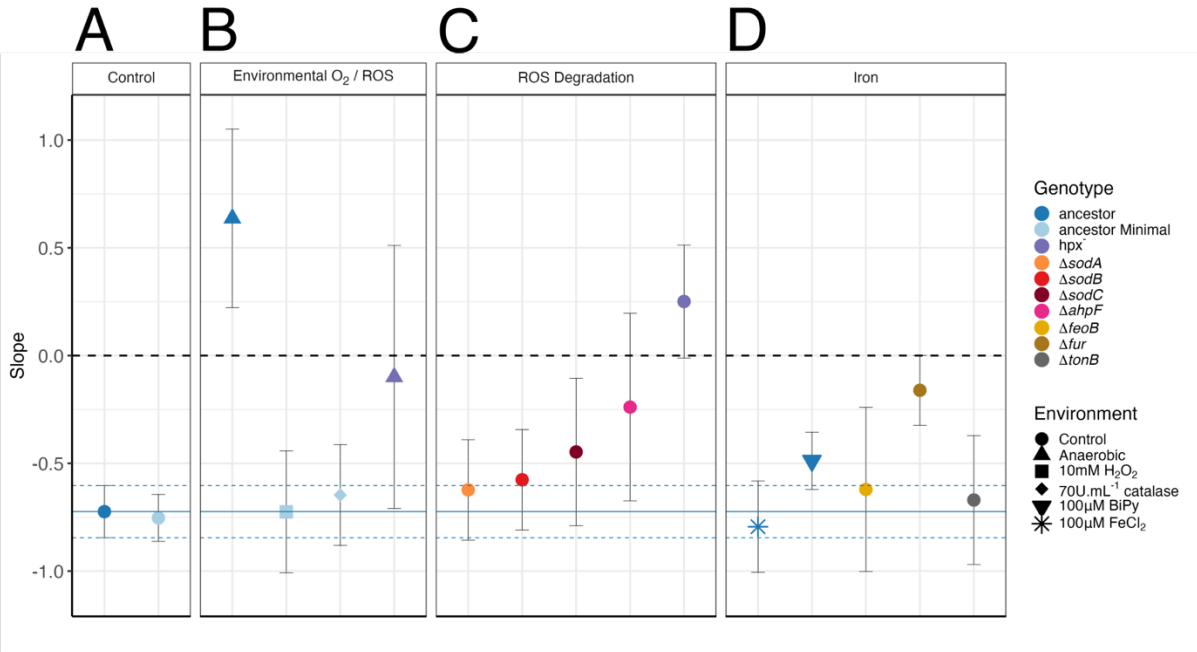

Figure 3: Mutation rate responses to population density in vivo under environmental and genetic manipulations. *Points show the slope of a log-log relationship between final population size and mutation rate (raw data shown in Fig. S4, Regression 4 (SI)), error bars show 95% CI on slope. Treatments shown are BW25113 ancestor (1106 parallel cultures (pc) across 69 fluctuation assays (fa)); ancestor minimal media (942 pc, 59 fa); ΔahpF (266 pc, 17 fa); hpx- (402 pc, 26 fa); ancestor anaerobic (168 pc, 11 fa); ancestor 10mM H_2O_2 (179 pc, 12 fa); ancestor 70U mL^{-1} catalase (167 pc, 11 fa); hpx- anaerobic (105 pc, 7 fa); ancestor + chelator 2,2,Bipyridyl 100μM (382 pc, 24 fa); ancestor + $FeCl_2$ 100μM*

(210 pc, 13 fa); ΔfeoB (192 pc, 12 fa); Δfur (504 pc, 31 fa); ΔtonB (113 pc, 7 fa). Dashed line shows a slope of 0 (no DAMP); solid blue line shows the slope of BW25113 ancestor in rich media with dashed blue lines showing 95% CI on this estimate (Regression 4 (SI)). All experiments were conducted in dilute LB media unless stated 'Minimal', in which case glucose minimal media was used.

Endogenous ROS degradation is necessary for DAMP *in vivo*

The second ODE model able to reproduce DAMP (model F) introduces increased rates of ROS degradation with increasing population density. If DAMP is the result of active cellular ROS degradation, we would expect strains deficient in this trait to lack DAMP. The two alkyl hydroperoxide reductase subunits AhpC and AhpF are together responsible for the majority of H_2O_2 scavenging in aerobically growing *E. coli* (24). The remaining H_2O_2 is degraded by the catalase enzymes HPI (*katG*) and HPII (*katE*) (25). The role of catalases in H_2O_2 scavenging is much more significant at high H_2O_2 concentrations due to the higher Michaelis constants of these enzymes, whereas AhpCF is saturated at ~20μM (25). We therefore estimated DAMP in a version of the *E. coli* MG1655 strain lacking *ahpC*, *ahpF*, *katG* and *katE* (hpx$^-$, (26)). This quadruple deletion results in a complete loss of DAMP with no significant change in the mutation rate across densities (slope = 0.25 ± 0.26 (95% CI), Fig. 3C, Regression 4 (SI)). Enzymatic degradation of H_2O_2 is thus essential to the DAMP phenotype, consistent with model F. Deleting only *ahpF* gives an intermediate DAMP phenotype (slope = -0.24 ± 0.44 (95% CI), Fig. 3C, Regression 4 (SI)) with significantly weaker DAMP than the wild-type (LR = 4.9, P = 0.028, Regression 4 (SI)), but still retaining stronger DAMP than hpx$^-$ (LR = 4.1, P = 0.043, Regression 4 (SI)), indicating that DAMP requires both catalase and alkyl-hydroperoxide reductase activity. In contrast, individual knockouts affecting superoxide rather than H_2O_2 (the superoxide dismutase genes *sodA, sodB and sodC,* slope = -0.62 ± 0.23, -0.58 ± 0.23, and -0.45 ± 0.34, respectively (95% CI), Fig. 3C, Regression 4 (SI)), or adding environmental H_2O_2 or catalase (slope = -0.73 ± 0.28, -0.65 ± 0.23, respectively (95% CI), Fig.3B, Regression 4 (SI)) do not significantly disrupt the wild-type negative relationship between population density and mutation rate (Table S1).

If the DAMP reproduced by model F is biologically realistic in this way, it requires that high-density populations, exhibiting reduced mutation rates, show greater efficiency at removing H_2O_2 from their environment than low-density populations. We measured external H_2O_2 in cultures after 24 hours of growth in rich or minimal media and found high-density populations to achieve significantly lower H_2O_2 concentrations (F_{28} = 24.3, P=3.3x10^{-5}, Regression 7B (SI), Fig. S6); there was no significant effect of rich versus minimal media (F_{26} = 0.77, P=0.39, Regression 7A (SI)). The reverse pattern is seen in sterile media where increasing nutrient provision leads to increased H_2O_2 concentration (F_{46} = 9.8, P = 3x10^{-3}, Regression 6 (SI)). This supports the hypothesis that, as required by model F, high-density populations detoxify external H_2O_2 better than low-density populations. However, while they are necessary, it does not require that all external H_2O_2 present in sterile media is degraded by alkyl-hydroperoxidase and catalase – other molecules, notably pyruvate, are excreted by *E. coli* with a substantial capacity for H_2O_2 degradation (27-29).

Cellular iron regulation is required for DAMP

Our model-guided hypothesis testing has shown that DAMP requires H_2O_2. Our models involve the direct effect of ROS on DNA, however, it's the reaction of free Fe(II) with H_2O_2 to produce mutagenic $OH^{\cdot}$ radicals, Fenton chemistry, which is a major source of oxidative stress in *E. coli* (30, 31). These radicals are far more reactive and damaging to DNA than H_2O_2 itself, making iron critical to determining the amount of damage H_2O_2 causes (32). If DAMP's dependence on H_2O_2, is the result of variable oxidative damage to DNA and nucleotides, we would expect this mutation rate plasticity to be perturbed by changes in cellular iron homeostasis. We first tested this using environmental

manipulations of iron. However, the provision of $FeCl_2$ or starving cells of iron with a chelator (2,2-bipyridyl), has little effect on DAMP (Fig. 3D). Nonetheless we find that a deletant of *fur*, the master regulator of intracellular iron, results in an almost constant mutation rate across cell densities, with a significant reduction in DAMP compared to the BW25113 wild-type (slope = -0.16 ± 0.16 (95% CI); wt slope comparison: $LR = 30.2$, $P = 3.9 \times 10^{-8}$, Regression 4 (SI)). Fur is a negative regulator of multiple iron importers (33), therefore in Δ*fur* strains the internal redox-active iron pool is elevated (34) leading to increased oxidative stress and DNA damage (35). Knockouts of the iron importer genes *feoB* and *tonB* , which, if anything, reduce intracellular iron (36, 37), do not lead to any change in mutation rate plasticity (Fig. 3D, Table S1), likely because regulators such as Fur are able to maintain iron homeostasis in the absence of these individual importers.

The critical contribution of iron to H_2O_2 stress is further demonstrated through whole genome sequencing of the hpx^- and strain used here. We find a 190bp loss-of-function mutation in the iron importer *fecD* (all mutations listed in Table. S2). This may have allowed this hpx^- strain to escape the positive feedback cycle that hpx^- cells experience, in which higher H_2O_2 concentrations prevent Fur from effectively limiting iron uptake, more intracellular free iron then further exacerbates the damage done by the excess H_2O_2 (38, 39). It is likely that this loss-of-function mutation is an adaptation, during laboratory culture, to the loss of Fur functionality caused by the oxidation of intracellular iron.

Wild-type cells restore DAMP in cells deficient in peroxide degradation

We have identified DAMP as requiring environmental H_2O_2 and iron regulation, where, with wild-type iron regulation, less H_2O_2 leads to lower mutation rates at higher final cell densities. This understanding leads us to predict that the presence of wild-type cells should restore DAMP in the peroxidase and catalase deficient hpx^- strain. It has previously been shown that a wild-type population can provide protection against environmental H_2O_2 to cocultured hpx^- cells, or similarly H_2O_2 sensitive Δ*oxyR* cells, through decreasing the peroxide concentration of the external environment (24, 40). To better distinguish hpx^- and wild-type strains in a coculture, two nalidixic acid (Nal) resistant strains of hpx^- were independently created with the resistance conferred by point mutations in *gyrA* (D87G & D87Y). Coculturing these hpx^-_{nalR} strains with wild-type BW25113 cells, the loss of DAMP via the hpx^- mutation (Fig. 3C) is phenotypically complemented by the wild-type cells. That is, hpx^-_{nalR} mutation rate is significantly decreased in coculture with increasing population density either of the hpx^- strain (Fig. 4, Fig. S7, slope = -0.93 ± 0.54 (95% CI), $X^2_{(DF=1)} = 10.9$, $P = 9.8 \times 10^{-4}$, Regression 4 (SI)), or total population density (Fig. S8, Slope = -1.4 ± 0.98 (95% CI), $t_{29} = -2.8$, $P = 9 \times 10^{-3}$, Regression 8 (SI)). This supports the hypothesis that DAMP is the result of reduced environmental H_2O_2 concentrations achieved by the local wild-type population.

Such mutation rate estimates in coculture could potentially be confounded by differential survival of rifampicin-resistant (RifR) mutants of hpx^-_{nalR} when plated in a monoculture or a coculture. In order to test for any differences in mutant survival we conducted a 'reconstruction test' (as in Fig. S13 of (21)); plating a predetermined number of $hpx^-_{nalR\&rifR}$ cells with a population of rifampicin susceptible hpx^- or wild-type cells on the selective rifampicin agar. No significant difference in plating efficiency was seen between plating with hpx^- vs. low, medium or high density of wild-type cells (Fig. S7; $LR_7 = 0.3$, $P = 0.96$, Regression 9 (SI)). Some difference in plating efficiency between the two $hpx^-_{nalR\&rifR}$ strains was observed (Fig. S9), this is likely due to the pleiotropic effects of RifR resistance mutations in the *rpoB* gene (41, 42).

Although the wild-type strain reintroduces a negative dependence of mutation rates on population density in hpx^-_{nalR} we also observe an increase in total hpx^-_{nalR} mutation rates (Fig. S8). This is potentially the result of out-competition by the wild-type strain leading hpx^-_{nalR} growth to stop

earlier in the culture cycle where, consistent with previous fluctuation results ((43), Chapter 5.4.3), our modelling leads us to expect higher mutation rates (Fig. 1D).

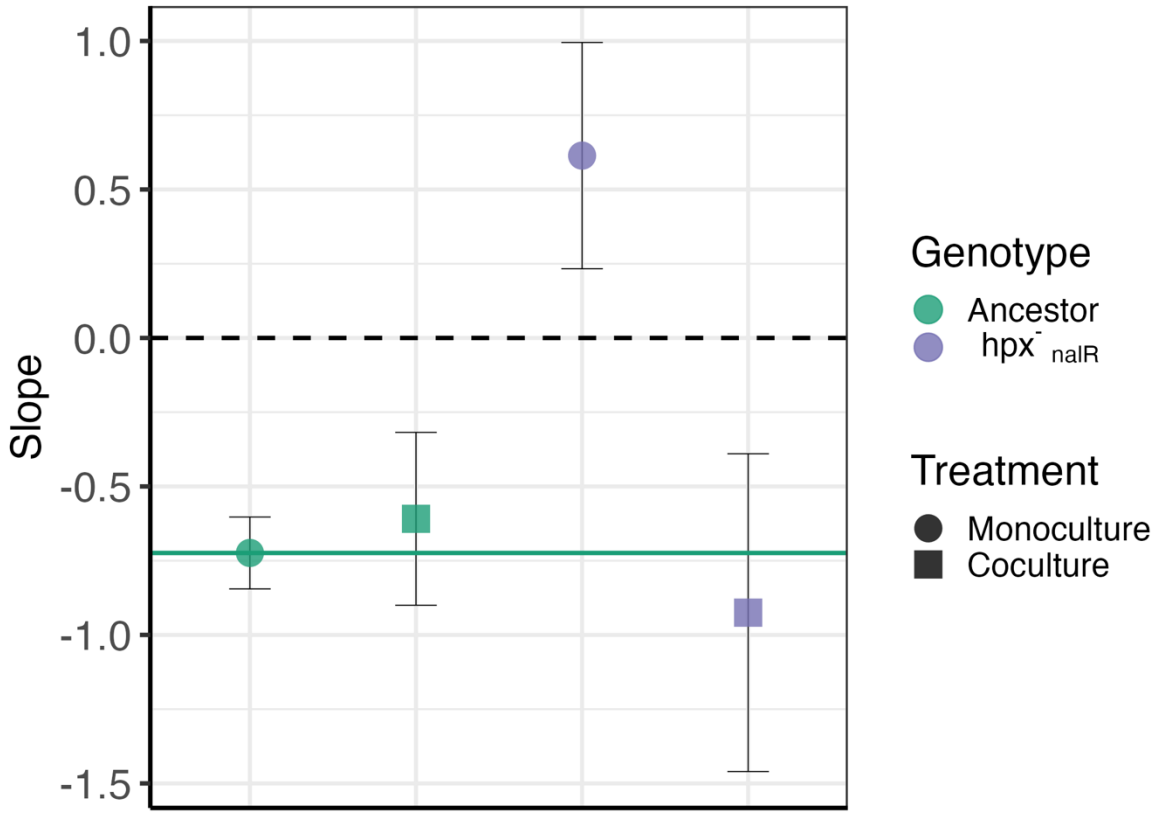

Figure 4: Coculture with wild-type cells restores DAMP in cells deficient in peroxide degradation: *points show log-log relationship between final population density of the focal strain and mutation rate fitted by regression 4 (SI) (raw data shown in Fig. S7), error bars show 95% CI on slope. We found no significant differences between independent* hpx^-_{nalR} *strains, therefore* hpx^- *strains D87Y & D87G are combined in* hpx^-_{nalR}*. Treatments shown are: BW25113 ancestor (1106 pc, 69 fa); BW25113 in coculture with* hpx^- *(498 pc, 31 fa);* hpx^-_{nalR} *(388 pc, 24 fa);* hpx^-_{nalR} *in coculture with BW25113 (319 pc, 20 fa).*

Discussion

Using ODE modelling (Fig. 1-2) to guide *in vivo* experiments in *E. coli* we have been able to predict and demonstrate the mechanisms behind the widespread phenomenon of reduced mutation rates at high microbial population densities (density-associated mutation rate plasticity, DAMP (3)). Genetic and environmental manipulations show that DAMP results from the improved degradation of H_2O_2 as the population density is increased (Fig. 3). The reintroduction of DAMP in catalase/peroxidase deficient cells by coculture with wild-type cells (Fig. 4) demonstrates the importance not only of a microbe's own population density in determining the mutation rate but also the density and genotype of coexisting populations. Our results demonstrate that mutation rates can be context dependent, through the degradation capacity of a community for mutagens including, but perhaps not limited to, H_2O_2. This collective protection from harmful molecules mirrors studies such as (44), demonstrating the importance of population structure in microbial ecology.

Increased population density provides protection against high levels of external H_2O_2 stress (40, 45, 46). However, the concentrations of 100µM-1mM applied in such studies is far beyond the range of known environmental concentrations, which is typically up to only 4µM (47). Here we show that without any external input of H_2O_2 higher density populations detoxify environmental H_2O_2 more effectively over 24 hours than low-density populations (Fig. S6). As well as improving survival under extreme H_2O_2 stress, previous work also finds mutation rates to decrease in cells protected by a higher density of neighbours able to detoxify the environment (40). Here we find that this mutation protection holds in the absence of external H_2O_2 application with the presence of higher density wild-type rescuers able to modify mutation rates in catalase/peroxidase deficient cells (Fig. 4). This interaction between two *E. coli* strains raises the question of whether similar effects will be seen in mixed species communities such as human microbiomes where mutations can be critical for medically important traits, such as antimicrobial resistance (48, 49). This study, and previous work on DAMP (3, 14, 21), considers *E. coli* batch culture in which there is no renewal of media, meaning that peroxide detoxification is permanent. As media inflow and outflow increase in a system, the ability of individual cells to detoxify ROS is decreased (50), it therefore seems possible that, increasing flow will be similar to transitioning from model D (fixed supply of environmental ROS, resulting in DAMP, Fig. 2) to model C (fixed level of environmental ROS, resulting in no DAMP, Fig. 2). That would mean that the spatial structuring and resulting fluid dynamics of flow, which can be critical for bacterial competition (44, 51), are also critical for mutation supply. Such factors vary greatly among natural environments, meaning that the effect of DAMP could be very different in low versus high through-flow environments (e.g. soil rather than water or lung rather than bladder). Tracing mutagenesis in single cells of spatially structured populations (52) has the potential to define the spatial scales and through flow conditions under which benefits from mutagen degradation are shared.

Our finding that oxygen is key to mutation rate plasticity is supported by mutation accumulation experiments showing that increased oxygen uptake is correlated with increased mutation rates (4). However, existing literature is not agreed on this point – anaerobic fluctuation assay-like experiments also report reduced mutation frequencies for resistance to multiple antibiotics (53), while anaerobic mutation accumulation experiments instead report increased mutation rates (54, 55). Work assessing mutation rate by the accumulation of resistance mutants in chemostats also shows oxygen limitation to reduce mutation rates relative to carbon limitation (10). This discrepancy is likely due to the change in mutational spectra caused by anaerobiosis: although overall mutation rates increase, base pair substitutions (BPS) fall in frequency by 6.4 times (54) and it is such BPS which we modelled computationally and are often responsible for antibiotic resistance (56-58), particularly to rifampicin, the drug we used for our mutation rate estimates (57). In line with our finding that iron and oxygen disruption are similarly able to abolish DAMP, iron and oxygen limitation produce similar mutational spectra (10). The loss of DAMP in the Δ*fur* strain is perhaps due to higher intracellular iron levels producing a greater rate of H_2O_2 breakdown into DNA-damaging radicals before it can be detoxified, reflective of ODE model C in which a constant ROS burden is applied and no DAMP seen.

Mutation supply is a key evolutionary hurdle often limiting the adaptation of populations (1, 59-61). As mutation supply depends on population size, one might expect the supply of mutations, for instance to AMR, to be severely limited in small populations, such as the small number of cells forming an infectious propagule of *E. coli* (17). Even when population size is sufficient to enable adaptation, mutation supply may have more subtle effects on the course of evolution, as demonstrated by the pervasive effects of mutational biases (62-64). However, due to the action of DAMP in elevating mutation rates at low density, small populations can experience a very similar supply of mutations to large populations (as demonstrated in our data, Fig. S4). For *E. coli* at least,

there is a limit to this effect as beyond intermediate densities (~7x10^8 CFU ml^{-1}) the action of stress-induced mutagenesis causes mutation rates to rise, rather than fall, with increased density (14).

The dependence of DAMP on active cellular control of H_2O_2 concentrations, uncovered here, helps explain it's highly conserved nature. The evolution of cellular systems in an anaerobic world for ~1 billion years (65) means that all branches of life are similarly vulnerable to damage by ROS, leading to parallel effects of ROS damage across life (66), potentially including its population level control in DAMP. Although DAMP is highly conserved, it is notably not seen in *Pseudomonas aeruginosa* (3), despite this species being a close relative of *E. coli.* How DAMP is lost between close evolutionary relatives remains an interesting question and is perhaps linked to the formation of multicellular aggregates by *P. aeruginosa* (67). Population associations with mutation rate are widespread, including a significant negative relationship between the effective population size and mutation rates across vertebrates (68) as well as microbes (69). Such patterns seem likely to be driven by the increased efficiency of natural selection against the deleterious effects of mutation in large populations (the drift barrier hypothesis, (70)), rather than any adaptive benefit. The broad reach of such non-adaptive explanations and the fact that the evolutionary effects of DAMP are yet to be explored means that any adaptive explanations should be approached with great caution. Nonetheless, in strains with DAMP, the mutation rate decreases as the absolute fitness increases, providing the greatest mutation supply to the most poorly performing populations (21). Mutation supply also rises in the most nutrient rich environments (14), perhaps providing greater evolutionary potential where competition is most intense. Such plausible evolutionary benefits of DAMP could exist, even if the ultimate origins of its conserved mechanism lie not in selection for its indirect effects via mutation, but in the legacy, across domains of life, of the chemistry of the Great Oxidation Event (71).

Materials & Methods

Ordinary differential equations: Model A

All variables (Fig. 1A, Table. 1) are measured in molar concentration within the cytoplasm, aside from the volume of that cytoplasm (***cytVol***), measured in mL, and external glucose (***eGlc***) and number of growing cells (***wtCell*** & ***mCell***) which are measured as molar concentrations within the 1ml batch culture. It is possible to convert between cytoplasmic and total metabolite concentrations through scaling by the cytoplasmic volume; this is calculated as the number of cells multiplied by a volume of 1.03 x 10^{-9} µl per cell (72). The reaction of ***dGTP*** with ***ROS*** creates oxidised dGTP (***odGTP***) which is then incorporated into DNA, creating AT > CG base pair substitution mutations (20). Mutations caused by ***odGTP*** may be avoided or repaired by the action of MutT, MutY and MutS enzymes (73). By dividing the number of mutant cells (***mCell***) by the total cell number (***mCell*** + ***WtCell***) at any point during the simulation, a mutation rate (bp^{-1} $generation^{-1}$) across the simulation up to that point, can be calculated.

Variable	Definition	Starting Value	Units	Region
eGlc	External glucose	3.1x10^{-4} to 6.2x10^{-3}	M	1mL culture
iGlc	Internal glucose	0	M	Cytoplasm
dGTP	Deoxyguanosine triphosphate	0	M	Cytoplasm

DNA	Guanine nucleotides in the newly synthesised strand	0	M	Cytoplasm
WtCell	Guanine nucleotides in the template strand	$8.5x10^{-12}$	M	1 mL culture
ROS	Reactive oxygen species (H_2O_2)	0	M	Cytoplasm
odGTP	8-oxo-2'-deoxyguanosine triphosphate	0	M	Cytoplasm
mDNA	odGTP nucleotides in the newly synthesised DNA strand	0	M	Cytoplasm
mCell	odGTP nucleotides in the template DNA strand	0	M	1 mL culture
cytVol	Total cytoplasmic volume	$2.25x10^{-9}$	mL	NA

Table 1: Definitions and starting values for the 10 variables in ODE model A. *For variables measured as a concentration, the volume within which this is calculated is given in the 'region' column. wtCell and cytVol starting values equate to 2175 cells (assuming 2357528 GC bp in the E. coli genome (strain MG1655, EBI Accession U00096.3) and cell volume of $1.03x10^{-12}$ mL (72)).*

The uptake of glucose is described by saturating Michaelis Menten kinetics whilst the oxidation of ***dGTP*** is described as a bimolecular reaction dependent on the cytoplasmic concentrations of ***dGTP*** and ***ROS***. All other steps are described by 1st order mass action kinetics in which the rate equals the concentration of the reactant multiplied by a rate constant (Eq. 1-10). The model is parameterised from published enzymatic and culture data alongside our own wet lab data (Table. 1).

R code to recreate all models and analysis is available as a supplementary file. All models were simulated in R (V4.3.1) (74) using package deSolve (V1.36) (75), logarithmic sequences were produced with emdbook (V1.3.13) (76), data handling and plotting was done using the tidyverse (V2.0.0) (77) and magrittr (V2.0.3) and parallel computing was done using parallel (V4.3.0), doParallel (V1.0.17) and foreach (V1.5.2). Linear mixed models were fitted to lab data with nlme (V3.1-162) (78), and plots formatted and coloured using cowplot (V1.1.1), gridExtra (V2.3), ggeffects (V1.3.1) (79) and RColorBrewer (V1.1-3). The flow diagram (Fig. 1A) was made using R package DiagrammeR (V1.0.10).

Parameter	Value	Units	Description	Source
U1	2.66E-01	$M^{-1}s^{-1}$	Maximum uptake rate (Vmax) of eGlc	Fitted from a known value of Ks (80) and data on *E. coli* growth dynamics (81) (Fig. S14).
M1	2.69E-04	s^{-1}	Rate of dGTP synthesis from iGlc	This value was fitted to published data on *E. coli* growth dynamics (81) (Fig. S14).

Ks	3.97E-05	M	Michaelis Menten constant K_s: Concentration of glucose at which glucose uptake rate of 1/2 Vmax is achieved	K_s measured as 7.16 µg/ml by (80).
I1	6.90E-03	s^{-1}	Rate of dGTP incorporation into DNA opposite C	Fitted to give known cytoplasmic concentration dGTP in exponential growth phase *E. coli* of 92 µM in 0.4% glucose (82).
D1	6.90E-03	s^{-1}	Rate of C pairing opposite incorporated G	Given the same value as I1 as the synthesis of new DNA (***DNA***) and new genomes (***wtCell***) should generally proceed at equal rates (this is violated during rapid exponential growth (83) but not included in this model).
O2	12.0	$M^{-1}s^{-1}$	Rate of dGTP oxidation to odGTP by ROS	Selected to give a mutation rate of $1.94x10^{-10}$ base pair substitutions per nucleotide in 0.2% glucose minimal media (20).
I2	2.53E-04	s^{-1}	Rate of odGTP incorporation into DNA opposite adenine	The relative efficiency of odGTP binding to A (I2) compared to G binding to C (I1) is $7.7x10^{-8}$: $2.1x10^{-6}$ (19) therefore I2 = I1 * ($7.7x10^{-8}/2.1x10^{-6}$).
D2	2.00E-04	s^{-1}	Rate of C pairing opposite incorporated oG causing an AT>CG mutation	Rate of C pairing opposite an odGTP (D2) relative to CG (I1 & D1) is $6x10^{-8}$:$2.1x10^{-6}$ (19).
C1	2.8	s^{-1}	Rate of odGTP hydrolysis to odGMP by nudix hydrolase enzyme MutT (NudA)	Value taken from Kcat of MutT measured *in vitro* (84).
C2	3.50E-04	s^{-1}	Rate of removal of adenine base incorporated opposite 8-oxodG in the genome by enzyme MutY	Value taken from Kcat of MutY measured *in vitro* as 0.021 min^{-1} = $3.5x10^{-4}$ sec^{-1} (85).

R1	2.00E-04	s^{-1}	Rate of oG insertion into DNA opposite cytosine	Relative incorporation efficiency opposite C of odGTP:dGTP (R1) is 0.029 (19), therefore R1 = I1 * 0.029 .
S	2.58E-02	s^{-1}	Rate of removal of adenine base incorporated opposite 8-oxodG in the genome by enzyme MutS	Fitted to known rate of mutation in *mutS* knockout of 40x wild-type (86).
r	17.3	s^{-1}	Rate of ROS production from iGlc relative to dGTP production rate	Selected to a known H_2O_2 production rate of 14 µM/second in 0.2% glucose minimal media normalised to cell volume (24).
O3	5.60E+01	s^{-1}	Rate of ROS degradation through reactions other than dGTP oxidation	Fitted to give a standing ROS concentration of $1.9x10^{-7}$ M, midpoint of known $1.3x10^{-7}$ - $2.5x10^{-7}$ M in LB (87).
R2	2.53E-04	s^{-1}	Rate of adenine pairing opposite incorporated oG	The relative efficiency of odGTP binding to A (R2) compared to G binding to C (I1) is $7.7x10^{-8}$: $2.1x10^{-6}$ (19) therefore R2 = I1 * ($7.7x10^{-8}$/$2.1x10^{-6}$).
Met1	1545	s^{-1}	Stoichiometry of glucose conversion to dGTP for genome building (i.e. how many molecules of glucose are needed to produce 1 molecule of dGTP)	Fitted to published data from (3) of cell density as a product of glucose concentration (Fig. S15).
CellVol	1.03E-12	mL	Volume of one *E. coli* cell in minimal media growing in	Mean value of 4 estimates of cell volume in exponential phase cells grown in minimal M9 media (72).

			exponential phase	
molML	6.02E+20	molecules	Number of molecules per mL in a 1M solution.	One thousandth of Avogadro's constant (N_A).
GCperGen	2357528	GC basepairs	Number of GC basepairs per genome.	*E. coli* Strain MG1655, EBI Accession U00096.3

Table 2. Parameter values and descriptions for all parameters used in model A.

$$[Eq.1]\ \frac{deGlc}{dt} = -U1\ \ Gcell\ \ \frac{eGlc}{eGlc + Ks}$$

$$[Eq.2]\ \frac{diGlc}{dt} = \frac{U1\ \ Gcell\ \frac{eGlc}{eGlc + Ks}}{cytVol} - Met1\ \ M1\ \ iGlc$$

$$[Eq.3]\ \frac{ddGTP}{dt} = M1\ \ iGlc - I1\ \ dGTP - dGTP \times ROS \times O2$$

$$[Eq.4]\ \frac{dDNA}{dt} = I1\ \ dGTP + C2\ mDNA + S\ mDNA + R1\ odGTP - D1\ DNA$$

$$[Eq.5]\ \frac{dGcell}{dt} = (D1\ \ DNA\ cytVol + R2\ \ mDNA) \times cytVol$$

$$[Eq.6]\ \frac{dcytVol}{dt} = (D1\ \ DNA\ cytVol + R2\ \ mDNA) \times cytVol \times \frac{molML}{GCperGen}\ CellVol$$

$$[Eq.7]\ \frac{dROS}{dt} = M1\ \ r\ \ iGlc - dGTP\ \ ROS\ \ \ O2 - O3\ \ ROS$$

$$[Eq.8]\ \frac{dodGTP}{dt} = dGTP\ \ ROS\ \ O2 - C1\ \ odGTP - I2\ \ odGTP - R1\ \ odGTP$$

$$[Eq.9]\ \frac{dmDNA}{dt} = I2\ \ \ odGTP - D2\ \ \ mDNA - C2\ \ \ mDNA - S\ \ mDNA - R2\ mDNA$$

$$[Eq.10]\ \frac{dmGcell}{dt} = D2\ \ mDNA\ \ \ cytVol$$

Equations 1-10: ODE equations for initial model (A)

Model Variants

Model B - Glucose uptake increases at low eGlc

Original Michaelis Menten kinetics are removed as this reverses the intended effect.

$$[Eq.1_B]\ \frac{deGlc}{dt} = -U1\ \ Gcell\ \ \frac{U2 - eGlc}{U2 - eGlc + K2}$$

$$U2 = 6.7e-3$$
$$K2 = 1.82e-4$$

Both U2 and K2 are in Molar units.

6.7x10^{-3} is chosen as a value slightly higher than maximum eGlc so that the value of $\frac{U2-eGlc}{U2-eGlc+K2}$ can cover almost a full range of 0 to 1. This means that glucose uptake rate will increase from almost 0 to 100% of the measured uptake rate as the external glucose concentration falls. K2 is given as 1.82x10^{-4} as this value produces the most negative DAMP slope achievable within the structure; values were tested from 1.82x10^{-6} to 1.82x10^{-2} (SI code file).

Model C - Constant ROS concentration uncoupled from metabolism

By decoupling ROS concentration from metabolism there is no extra production of ROS in cells grown to higher density, we expect this to prevent a positive DAMP slope.

$$[Eq.8_C]\frac{dodGTP}{dt} = dGTP\ \ ROSC\ \ O2 - C1\ \ odGTP - I2\ \ odGTP - R1\ \ odGTP$$

$$ROSC = 1.8e-7$$

ROSC in Molar units

ROS is removed as a variable and replaced with a constant concentration of 1.8x10^{-7}, this is within the known internal ROS concentration of 1.3x10^{-7} - 2.5x10^{-7} M (87) and produces mutation rate of 1.93x10^{-10} based on lab data and (20).

Model D - Constant ROS production regardless of population density

By creating a situation in which ROS is produced in the media at a constant rate (e.g. (22)) and then taken up among all present cells, higher density populations will expose each individual cell to less ROS. We expect this to create negative a DAMP slope as more mutagenic ROS exists inside the cells of low-density populations. This structure may be reflective of a situation in which iron is limited and so higher density populations have less iron per cell. Because of the role of iron in the Fenton reaction it may be expected that less iron leads to less ROS damage in the cells, as observed by (88).

$$[Eq.7_D]\frac{dROS}{dt} = \frac{ROSC2}{cytVol} - dGTP\ \ ROS\ \ O2 - O3\ \ ROS$$

$$ROSC2 = 2e-10$$

ROSC2 in Molar units

ROSC2 defines the number of millimoles of hydrogen peroxide produced in the system each second, this is split between the cytoplasm of all cells. The chosen value of 2x10^{-10} creates a H_2O_2 production rate at 76% of that expected from (24) and a mutation rate 96.8% of that expected from (20).

Model E - ROS removal dependent on internal glucose

We expect greater rates of ROS removal to lead to lower rates of GTP oxidation, and therefore lower mutation rates. If ROS is more able to be degraded when resources are abundant this may produce DAMP.

$$[Eq.7_E]\ \frac{dROS}{dt} = M1\ r\ iGlc - dGTP\ ROS\ O2 - O3\ ROS\ \frac{iGlc}{iGlc + C3}$$

$$C3 = 1.5e-4$$

C3 is in Molar units

C3 is adjusted to produce known mutation rate of 1.98x10^{-10} base pair substitutions per nucleotide in 0.2% glucose minimal media (20).

Model F - ROS removal dependent on population density

We expect direct control of ROS degradation by population density to allow cells in higher density populations to avoid mutations more efficiently.

$$[Eq.7_F]\ \frac{dROS}{dt} = M1\ r\ iGlc - dGTP\ ROS\ O2 - ROS\ \frac{MolML}{GCperGen}\ Gcell\ C3a$$

$$C3a = 3.5e-6$$

C3a is in Sec^{-1} units.

C3a of 3.5x10^{-6} is chosen to reproduce the mutation rate of 2.05x10^{-10} base pair substitutions per nucleotide.

Model G - MutT activity upregulated by internal glucose

MutT activity is known to be essential to DAMP and so density dependent MutT activity is a candidate DAMP mechanism. iGlc accumulates at higher levels in cells growing to high density, we expect high MutT activity in these cells to lead to a reduced mutation rate due to MutT cleaning of odGTP.

$$[Eq.8_G]\ \frac{dodGTP}{dt} = dGTP\ ROS\ O2 - C1\ \frac{odGTP}{1 - \frac{iGlc}{C3G}} - I2\ odGTP$$

$$C3G = 2.6e-3$$
$$O2 = 70$$

C3G is in Molar units.

2.6x10^{-3} is selected as a number slightly higher than the maximum iGlc achieved (~0.0023), this prevents MutT activity levels from falling below 0. O2 is refitted to 70 to restore desired mutation rate.

Model H - MutT activity upregulated by odGTP

If MutT activity is actively upregulated to degrade odGTP at a higher rate upon exposure to higher odGTP concentrations, then we expect cells grown in higher glucose, with higher internal metabolite concentrations, to have a greater ability to evade mutations caused by odGTP.

$$[Eq.8_H]\ \frac{dodGTP}{dt} = dGTP\ \ ROS\ \ O2 - C1\ \frac{odGTP}{1-\frac{odGTP}{C3b}} - I2\ \ odGTP$$

$$C3b = 8e-10$$

C3b is in Molar units.

$8x10^{-10}$ is selected as a number slightly higher than the maximum odGTP achieved, this prevents MutT activity levels from falling below 0.

Model I - MutT activity upregulated by ROS

Reasoning and value selection as in Models G/H

$$[Eq.8_I]\ \frac{dodGTP}{dt} = dGTP\ \ ROS\ \ O2 - C1\ \frac{odGTP}{1-\frac{ROS}{C3c}} - I2\ \ odGTP$$

$$C3c = 1.98e-7$$
$$O2 = 130$$

C3c is in Molar units.

Model J - Michaelis Menten MutT kinetics

Michaelis Menten kinetics describe saturating, enzyme catalysed reactions. In this situation reaction rates proceed slower at low substrate concentrations rising to an asymptote at maximum reaction rate. As with models G/H/I we expect this to reduce mutation rates by increasing MutT activity in high density populations with greater internal metabolite concentrations.

$$[Eq.8_J]\ \frac{dodGTP}{dt} = dGTP\ \ ROS\ \ O2 - C1\ \ odGTP\ \ \frac{odGTP}{odGTP+Kt} - I2\ \ odGTP$$

$$Kt = 0.48$$
$$O2 = 6.97e-4$$

Kt is in Molar units.

Kt value given by (19), O2 is then titrated to restore mutation rate as in (20).

Model K – Separated activity of ahpCF and katEG genes + limited diffusion of ROS across the plasma membrane

$$[Eq.7_{KA}]\frac{dROS_{internal}}{dt} = M1\ \ r\ \ iGlc\ -\ dGTP\ \ ROS\ \ \ O2\ -\ \frac{kAhp\ ROS}{ROS + kmAhp} - \frac{kKat\ ROS}{ROS + kmKat} - kdiff\ (ROS_{internal} - ROS_{external})$$

$$[Eq.7_{KB}]\frac{dROS_{external}}{dt} = kdiff\ (ROS_{internal} - ROS_{external})(\frac{cytVol}{1 - cytVol})$$

As in (23) the activity of alkylhyrdoperoxidase and catalase proteins are separated to allow for their specialisations to low and high H_2O_2 concentrations respectively. Michaelis Menten constants are as follows:

$$kAhp = 6.6e-4$$
$$kmAhp = 1.2e-6$$
$$kKat = 4.9e-1$$
$$kmKat = 5.9e-3$$

All in Molar units.

Permeability coefficient, diffusion coefficient and cell surface area are taken from (23) to calculate the diffusion coefficient as follows:

$$kdiff = \frac{permeability\ \times surface\ area}{volume} = \frac{1.6 \times 10^{-3} cm\ s^{-1}\ \times 1.41\ \times 10^{-7} cm^2}{3.2\ \times\ 10^{-12}\ cm^3} = 70$$

kdiff is in is in Sec^{-1} units

H2O2 production rate and standing concentration are restored to expected values by altering the value of r:

$$r = 175$$

Global Sensitivity Analysis

For each parameter within each model, 50,000 values between 10% to 1000% of the baseline value (Table. 2), spaced evenly along a log scale were tested. The set of values for each individual parameter were then independently shuffled so that no parameters were corelated with one another; allowing for substantial exploration of the available parameter space. Of these 50,000 parameter sets some encountered fatal errors in the ODE solver and so did not produce a DAMP slope estimate, the number of parameter sets run without fatal error is shown in Table 3 as 'complete'. Results were filtered for the following criteria: 1) Stationary phase is reached in all glucose conditions (defined as an average increase of less than 1 cell per 10 second time step across the last 1000 time steps (2.7 hours) of the simulation), 2) final population size >1x10^7 & <1x10^{10} at every glucose condition, 3) final population size increases with each increase in glucose concentration, 4) mutation rate >2x10^{-12} & <2x10^{-8} at all glucose conditions and 5) log-log relationship between mutation rate and final population size is substantially linear (defined by R-squared > 0.5). After this filtering the following number of parameter sets were retained for each model (Table 3).

Model	Complete	Filtered
A	49971	12261

B	33274	5444
C	49988	13496
D	49990	7128
E	49555	10267
F	49982	10115
G	23311	2730
H	49900	2210
I	22832	3334
J	49994	11741
K	45558	7365

Table 3: Counts of completed and filtered simulations from 50,000 parameter sets produced for global sensitivity analysis for each model variant. *'Complete' column lists the number of these parameter sets that were able to be simulated without fatal error from the ODE solver. 'Filtered' column lists how many parameter sets remained after filtering as described above.*

Strains used in this study

The parent of the Keio collection is *E. coli* strain BW25113 (F-, Δ(*araD*-araB)567, Δ*lacZ*4787 (::*rrnB*-3), λ-, *rph*-1, Δ(*rhaD-rhaB*)568, *hsdR*514). *E. coli* hpx$^-$ LC106 mutant is Δ*ahpCF*' kan:: Δ*ahpF* Δ (*katG*17::Tn10)1 Δ (*katE*12::Tn10)1 (26). *E. coli* single gene knockouts Δ*fur*, Δ*feoB*, Δ*tonB* and Δ*ahpF* are sourced from the Keio collection (89). *E. coli* K-12 strain MG1655 is from Karina B. Xavier. Nalidixic acid resistant strains hpx$^-$ (*gyrA* D87Y) & hpx$^-$ (*gyrA* D87G) were isolated from independent fluctuation assays of the original hpx$^-$ strains on 30 mg L^{-1} nalidixic acid selective plating.

Strains Δ*fur*, Δ*feoB*, Δ*tonB*, Δ*ahpF*, hpx$^-$, hpx$^-_{nalR}$(D87Y) and hpx$^-_{nalR}$(D87G) were sequenced to 30x depth by MicrobesNG to verify gene deletions. Lack of KatE activity in hpx$^-$ was verified by covering a colony on TA agar with 30% H_2O_2 with no bubbles of oxygen observed (as in (25)), the MG1655 wild-type was used as a positive control. Mutations were identified using breseq version 0.36.0 (90, 91) with bowtie2 version 2.4.1 and R version 4.2.0 and are listed in Table. S2. For hpx$^-$ strains the reference genome used was the *E. coli* K-12 MG1655 genome [(92), NCBI accession U00096.3]. For Keio knockout strains the reference genome used was the *E. coli* K-12 BW25113 genome [(93), NCBI accession CP009273.1], with additional annotations for insertion (IS) element regions to improve the calling of mutations related to IS insertion (modified Genbank format file as file S1 in (1)).

Media

We used Milli-Q water for all media, all chemicals are supplied by Sigma-Aldrich unless stated otherwise. LB medium contained: 10 g of NaCl (Thermo Fisher Scientific), 5 g of yeast extract (Thermo Fisher Scientific) and 10 g of tryptone (Thermo Fisher Scientific) per litre. DM medium contained 0.5 g of $C_6H_5Na_3O_7 \cdot 2H_2O$, 1 g of $(NH_4)2SO_4$ (Thermo Fisher Scientific), 2 g of H_2KO_4P and 7 g of $HK_2O_4P \cdot 3H_2O$ per litre; 100 mg L^{-1} $MgSO_4 \cdot 7H_2O$ (406 µmol) and 4.4 µg L^{-1} thiamine hydrochloride were added to DM after autoclaving. Selective tetrazolium arabinose agar (TA) medium contained 10 g of tryptone, 1 g of yeast extract, 3.75 g of NaCl and 15 g bacto agar per litre; after autoclaving 3 g of arabinose and 0.05 g of 2,3,5-triphenyl-tetrazolium chloride were added per litre, this was supplemented with freshly prepared rifampicin (50 µg ml^{-1}) or nalidixic acid (30 µg ml^{-1}) dissolved in 1mL of methanol or 1M NaOH respectively when required. For all cell dilutions sterile saline (8.5 g L^{-1} NaCl) was used.

Fluctuation Assays

Fluctuation tests were conducted as described in (94). Briefly; initial growth of glycerol stocks in LB was carried out for 4 hrs for all strains aside from hpx$^-$ which was grown for 7 hrs due to its reduced growth rate. A dilution factor of 1000x was then used for transfer to overnight cultures. Overnight acclimatisation was carried out in DM supplemented with 3.5% LB or 250mg L^{-1} glucose with nutrient type matching that of the fluctuation assay. The density achieved in the assay was manipulated by growth in varying nutrient conditions, either 2 - 5% LB diluted in DM or 80 - 1000 mg glucose L^{-1}. Selective plates were prepared 48 hours before use and stored for 24 hours at room temperature followed by 24 hours at 4ºC. All strains were plated on rifampicin selective media.

Anaerobic conditions were produced by incubating the 96 deep well plates in an airtight 2.6L container with one Anaerogen 2.5L sachet (Thermo Scientific). The Anaerogen sachet rapidly absorbs oxygen and releases CO_2 creating anaerobic conditions. Aerobic plates of matching design were grown in an identical container ventilated with 8 x 4mm diameter holes without Anaerogen sachet. In these plates 2-4 wells in each 96 well plate contained DM supplemented with 2.5% LB, resazurin and *E. coli* MG1655, leaving space for fluctuation assays of 15-16 parallel cultures. On removing the 96 well plates from incubation the resazurin absorbance at 670 nm was measured; this quantifies the change from pink resorufin (aerobic cell growth) to clear dihydro resorufin (anaerobic cell growth) thus providing an objective measure of anaerobiosis (Fig. S12).

During coculture fluctuation assays between BW25113 wild-type and hpx$^-$ both strains were grown up in LB, diluted LB overnight and diluted into cultures of ~$1x10^3$ CFU mL^{-1} as above. Some combination of these 2 initial cultures was then mixed in each parallel culture ranging from an hpx$^-$:wild-type ratio of 1:1 to 124:1 (recorded in the supplementary data file as 'Mut_to_WT_ratio'). Plating of these cultures on TA or TA+Rif agar enabled the Ara+ (white) hpx$^-$ colonies and the Ara- (red) wind-type colonies to be distinguished. For assays using NalR hpx$^-$ strains, selective plating was done on TA+Rif+Nal plates and so only hpx$^-$ mutants and not wild-type mutants were counted, Nt was determined for both strains using plating on both TA+Nal and TA. Due to amino acid synthesis defects, hpx$^-$ cells cannot be cultured in glucose minimal media and so all cocultures were conducted in dilute LB media (30).

In order to test for any differences in survival of hpx$^-$ (NalR) grown in monoculture VS with differing densities of BW25113 wild-type cells we conducted a reconstruction test (Fig. S9). A known quantity of hpx$^-$ (NalR + RifR) cells were plated with one of the following treatments: wild-type supernatant (3.5%LB overnight growth), sterile DM, 80U mL^{-1} catalase, hpx$^-$ (5%LB overnight growth), wild-type (2.5%LB overnight growth), wild-type (3.5%LB overnight growth), wild-type (5% overnight growth). Raw data from the reconstruction test is available in the supplementary R code file.

Though fluctuation assays allow for high-throughput and low-cost estimates of mutation rate, they classically come with some important assumptions to consider (95). For example, the assumption that resistance markers will be selectively neutral is not reasonable in practice (42). Fortunately, this can be accounted for with the estimation of fitness cost which can then be accounted for in the estimation of mutational events using R package flan (V0.9). We find estimations of DAMP with the co-estimation of the individual fitness cost in each assay or with the application of the median mutant:wild-type fitness ratio estimation (median = 0.57, Fig. S3) to have no effect on our conclusions. In regression 4 (SI), re-running the model using either of these approaches to account for genotypes having different competitive fitness makes no difference to whether DAMP is inferred (i.e. categorising each treatment as DAMP, no DAMP or reverse DAMP, Table S1) for all treatments. In this study we allow flan to co-estimate fitness along with mutational

events (*m*) for each assay. Occasionally this model failed to converge on estimates, in these cases average fitness effects were estimated from a model fitted to all successful estimates (Regression 3 (SI)) and then used to estimate *m* from the data with this pre-determined fitness effect of mutation. It is also possible to avoid issues of mutant fitness effects by using the p_0 method of estimation (95, 96) in which parallel cultures are simply divided into those with or without any viable mutants. However, this method is more restrictive as only assays in which parallel cultures both with and without growth have been observed can the method be applied, it is also subject to more error on estimates than maximum-likelihood methods. Reanalysing our data with the p_0 method shows DAMP to exist in the same set of treatments as in the original analysis (Fig. S11), discounting any effect of mutant fitness costs on our conclusions. Another potentially unrealistic assumption of the fluctuation assay is that there will be no death, this too is possible to account for using the tools provided in 'flan'. We find that death rates as high as 10%, well beyond what would be expected under our conditions which lack added stressors, cause no changes in DAMP category (Fig. S13).

Hydrogen Peroxide Measurement

External hydrogen peroxide is measured using the Amplex UltraRed (AUR)/Peroxidase assay as described in (22). All reagents were dissolved in 50 mM dibasic potassium phosphate. Diethylenetetraaminepentaacetic acid (DTPA) and AUR solutions were corrected to pH 7.8 with HCl or NaOH. Reactions containing 660 µL 1mM DTPA, 80 uL filter sterilised sample solution and 20 µL 0.25 mM AUR were mixed by vortexing before transferring 141 uL to three wells of a clear bottomed black 96-well plate. Fluorescence was measured at 580 nm excitation, 610 nm emission before and after the injection of 7.5 µL horseradish peroxidase (0.25 mg mL^{-1}) to each well, net fluorescence was calculated as initial fluorescence subtracted from final fluorescence. H_2O_2 concentration was estimated by calibration to standard solutions of 5 & 20 µM H_2O_2 (Regression 5 (SI)). Because of background levels of fluorescence, some predicted concentrations were negative, this was accounted for by taking the absolute value of the lowest prediction and adding this to all predictions. The range of H_2O_2 concentrations we observed is in good agreement with similar measurements in the literature (e.g. Fig. 6B in (22)).

Statistical Analysis

All statistical analysis was executed in R (V4.3.1) (74) using the nlme (V3.1-162) package for linear mixed effects modelling (78). This enabled the inclusion within the same regression of experimental factors (fixed effects), blocking effects (random effects) and factors affecting variance (giving heteroscedasticity). R package car (V3.1.2) (97) was used to carry out Chi-squared tests comparing slope to a null-hypothesis of 1 (Table. S1). In all cases $\log_2$ mutation rates were used. Details of all regression models are given supplementary statistical methods along with diagnostic plots and ANOVA tables for each model. The code and data to reproduce the main text figures are given in the accompanying R script, and supplementary data files, respectively. The content of the supplementary data files is explained in Table. S3. Standard deviation on estimates of *m* is calculated as in (98). The same R packages were used for parallel computing, data handling and plotting as for the ODE modelling, with the addition of plyr (V1.8.8), ggbeeswarm (V0.7.2) and gridExtra (V2.3).

Acknowledgements

Thanks to Danna Gifford for many insightful discussions during this study and for the improved BW25113 reference genome. Thanks also to The University of Manchester Research IT for their assistance and the use of the Computational Shared Facility. Thanks to MicrobesNG

(http://www.microbesng.com) for their genome sequencing services. Thanks to Simon C. Andrews for providing the hpx$^-$ strain and to Karina B. Xavier for providing the MG1655 wild-type strain.

References

1. Gifford DR, Berrios-Caro E, Joerres C, Sune M, Forsyth JH, Bhattacharyya A, et al. Mutators can drive the evolution of multi-resistance to antibiotics. PLoS Genet. 2023;19(6):e1010791.
2. Ragheb MN, Thomason MK, Hsu C, Nugent P, Gage J, Samadpour AN, et al. Inhibiting the Evolution of Antibiotic Resistance. Mol Cell. 2019;73(1):157-65 e5.
3. Krašovec R, Richards H, Gifford DR, Hatcher C, Faulkner KJ, Belavkin RV, et al. Spontaneous mutation rate is a plastic trait associated with population density across domains of life. PLoS Biol. 2017;15(8):e2002731.
4. Chu XL, Zhang BW, Zhang QG, Zhu BR, Lin K, Zhang DY. Temperature responses of mutation rate and mutational spectrum in an Escherichia coli strain and the correlation with metabolic rate. BMC Evol Biol. 2018;18(1):126.
5. Maharjan RP, Ferenci T. The impact of growth rate and environmental factors on mutation rates and spectra in *Escherichia coli*. Environ Microbiol Rep. 2018;10(6):626-33.
6. Liu H, Zhang J. Yeast Spontaneous Mutation Rate and Spectrum Vary with Environment. Curr Biol. 2019;29(10):1584-91 e3.
7. MacLean RC, Torres-Barcelo C, Moxon R. Evaluating evolutionary models of stress-induced mutagenesis in bacteria. Nat Rev Genet. 2013;14(3):221-7.
8. Foster PL. Stress-induced mutagenesis in bacteria. Crit Rev Biochem Mol Biol. 2007;42(5):373-97.
9. Loewe L, Textor V, Scherer S. High Deleterious Genomic Mutation Rate in Stationary Phase of *Escherichia coli*. Science. 2003;302(5650):1558-60.
10. Maharjan RP, Ferenci T. A shifting mutational landscape in 6 nutritional states: Stress-induced mutagenesis as a series of distinct stress input–mutation output relationships. PLoS Biol. 2017;15(6):e2001477.
11. Cirz RT, Chin JK, Andes DR, de Crecy-Lagard V, Craig WA, Romesberg FE. Inhibition of mutation and combating the evolution of antibiotic resistance. PLoS Biol. 2005;3(6):e176.
12. Domenech A, Brochado AR, Sender V, Hentrich K, Henriques-Normark B, Typas A, et al. Proton Motive Force Disruptors Block Bacterial Competence and Horizontal Gene Transfer. Cell Host & Microbe. 2020;27(4):544-55.e3.
13. Alam MK, Alhhazmi A, DeCoteau JF, Luo Y, Geyer CR. RecA Inhibitors Potentiate Antibiotic Activity and Block Evolution of Antibiotic Resistance. Cell Chem Biol. 2016;23(3):381-91.
14. Krašovec R, Richards H, Gifford DR, Belavkin RV, Channon A, Aston E, et al. Opposing effects of final population density and stress on *Escherichia coli* mutation rate. ISME J. 2018;12(12):2981-7.
15. Gifford DR, Bhattacharyya A, Geim A, Marshall E, Krašovec R, Knight CG. Environmental and genetic influence on rate and spectrum of spontaneous mutations in *Escherichia coli* bioRxiv:10.1101/2023.04.06.535897v3 [Preprint]. 2023 [cited 2023 September 06]. Available from: https://www.biorxiv.org/content/10.1101/2023.04.06.535897v3.
16. Tenaillon O, Skurnik D, Picard B, Denamur E. The population genetics of commensal *Escherichia coli*. Nat Rev Microbiol. 2010;8(3):207-17.
17. Cornick NA, Helgerson AF. Transmission and Infectious Dose of *Escherichia coli* O157:H7 in Swine. Applied and Environmental Microbiology. 2004;70(9):5331-5.
18. Imlay JA. Pathways of Oxidative Damage. Annual Review of Microbiology. 2003;57(1):395-418.
19. Maki H, Sekiguchi M. MutT protein specifically hydrolyses a potent mutagenic substrate for DNA synthesis. Nature. 1992;355(6357):273-5.
20. Foster PL, Lee H, Popodi E, Townes JP, Tang H. Determinants of spontaneous mutation in the bacterium *Escherichia coli* as revealed by whole-genome sequencing. Proc Natl Acad Sci U S A. 2015;112(44):E5990-9.

21. Krašovec R, Belavkin RV, Aston JA, Channon A, Aston E, Rash BM, et al. Mutation rate plasticity in rifampicin resistance depends on *Escherichia coli* cell-cell interactions. Nat Commun. 2014;5:3742.
22. Li X, Imlay JA. Improved measurements of scant hydrogen peroxide enable experiments that define its threshold of toxicity for *Escherichia coli*. Free Radic Biol Med. 2018;120:217-27.
23. Uhl L, Dukan S. Hydrogen Peroxide Induced Cell Death: The Major Defences Relative Roles and Consequences in *E. coli*. PLOS ONE. 2016;11(8):e0159706.
24. Seaver LC, Imlay JA. Hydrogen peroxide fluxes and compartmentalization inside growing *Escherichia coli*. J Bacteriol. 2001;183(24):7182-9.
25. Seaver LC, Imlay JA. Alkyl Hydroperoxide Reductase Is the Primary Scavenger of Endogenous Hydrogen Peroxide in *Escherichia coli*. J Bacteriol. 2001;183(24):7173-81.
26. Seaver LC, Imlay JA. Are Respiratory Enzymes the Primary Sources of Intracellular Hydrogen Peroxide? J Biol Chem. 2004;279(47):48742-50.
27. Korshunov S, Imlay JA. Two sources of endogenous hydrogen peroxide in *Escherichia coli*. Mol Microbiol. 2010;75(6):1389-401.
28. O'Donnell-Tormey J, Nathan CF, Lanks K, DeBoer CJ, de la Harpe J. Secretion of pyruvate. An antioxidant defense of mammalian cells. J Exp Med. 1987;165(2):500-14.
29. Kreth J, Lengeler JW, Jahreis K. Characterization of pyruvate uptake in *Escherichia coli* K-12. PLOS ONE. 2013;8(6):e67125.
30. Jang S, Imlay JA. Micromolar Intracellular Hydrogen Peroxide Disrupts Metabolism by Damaging Iron-Sulfur Enzymes. J Biol Chem. 2007;282(2):929-37.
31. Imlay JA, Chin SM, Linn S. Toxic DNA Damage by Hydrogen Peroxide through the Fenton Reaction in vivo and in vitro. Science. 1988;240(4852):640-2.
32. Park S, You X, Imlay JA. Substantial DNA damage from submicromolar intracellular hydrogen peroxide detected in Hpx$^-$ mutants of *Escherichia coli*. Proc Natl Acad Sci U S A. 2005;102(26):9317-22.
33. Seo SW, Kim D, Latif H, O'Brien EJ, Szubin R, Palsson BO. Deciphering Fur transcriptional regulatory network highlights its complex role beyond iron metabolism in *Escherichia coli*. Nat Commun. 2014;5(1):4910.
34. Keyer K, Imlay JA. Superoxide accelerates DNA damage by elevating free-iron levels. Proc Natl Acad Sci U S A. 1996;93(24):13635-40.
35. Touati D, Jacques M, Tardat B, Bouchard L, Despied S. Lethal oxidative damage and mutagenesis are generated by iron in delta *fur* mutants of *Escherichia coli*: protective role of superoxide dismutase. J Bacteriol. 1995;177(9):2305-14.
36. Gerken H, Vuong P, Soparkar K, Misra R. Roles of the EnvZ/OmpR Two-Component System and Porins in Iron Acquisition in *Escherichia coli*. mBio. 2020;11(3).
37. Qiu N, Misra R. Overcoming Iron Deficiency of an *Escherichia coli tonB* Mutant by Increasing Outer Membrane Permeability. J Bacteriol. 2019;201(17).
38. Varghese S, Wu A, Park S, Imlay KRC, Imlay JA. Submicromolar hydrogen peroxide disrupts the ability of Fur protein to control free-iron levels in *Escherichia coli*. Mol Microbiol. 2007;64(3):822-30.
39. Guyet A, Dade-Robertson M, Wipat A, Casement J, Smith W, Mitrani H, et al. Mild hydrostatic pressure triggers oxidative responses in *Escherichia coli*. PLOS ONE. 2018;13(7):e0200660.
40. Choudhary D, Lagage V, Foster KR, Uphoff S. Phenotypic heterogeneity in the bacterial oxidative stress response is driven by cell-cell interactions. Cell Reports. 2023;42(3):112168.
41. Maharjan R, Ferenci T. The fitness costs and benefits of antibiotic resistance in drug-free microenvironments encountered in the human body. Environ Microbiol Rep. 2017;9(5):635-41.
42. Soley JK, Jago M, Walsh CJ, Khomarbaghi Z, Howden BP, Lagator M. Pervasive genotype-by-environment interactions shape the fitness effects of antibiotic resistance mutations. Proc R Soc B Biol Sci. 2023;290(2005):20231030.

976 43. Richards H. Evolution of Evolvability? Understanding Mutation Rate Plasticity [Doctoral
977 Thesis]. https://www.research.manchester.ac.uk/portal/en/theses/evolution-of-evolvability-
978 understanding-mutation-rate-plasticity(2d8e5e78-dcd7-4d8c-b37e-07da62592644).html: The
979 University of Manchester; 2018.
980 44. Krishna Kumar R, Meiller-Legrand TA, Alcinesio A, Gonzalez D, Mavridou DAI, Meacock OJ, et
981 al. Droplet printing reveals the importance of micron-scale structure for bacterial ecology. Nat
982 Commun. 2021;12(1):857.
983 45. Ma M, Eaton JW. Multicellular oxidant defense in unicellular organisms. Proc Natl Acad Sci U
984 S A. 1992;89(17):7924-8.
985 46. Holland M, Farinella DN, Cruz-Lorenzo E, Laubscher MI, Doakes DA, Ramos MA, et al. L.
986 pneumophila resists its self-harming metabolite HGA via secreted factors and collective peroxide
987 scavenging. mBio. 2023:e0120723.
988 47. Sen A, Imlay JA. How Microbes Defend Themselves From Incoming Hydrogen Peroxide. Front
989 Immunol. 2021;12:667343.
990 48. Denamur E, Matic I. Evolution of mutation rates in bacteria. Mol Microbiol. 2006;60(4):820-
991 7.
992 49. Frapwell CJ, Howlin RP, Soren O, McDonagh BT, Duignan CM, Allan RN, et al. Increased rates
993 of genomic mutation in a biofilm co-culture model of *Pseudomonas aeruginosa* and *Staphylococcus*
994 *aureus* biorXiv:10.1101/387233v1 [Preprint]. 2018 [cited 2023 September 06]. Available from:
995 https://www.biorxiv.org/content/10.1101/387233v1.full.
996 50. Padron GC, Shuppara AM, Sharma A, Koch MD, Palalay J-JS, Radin JN, et al. Shear rate
997 sensitizes bacterial pathogens to H_2O_2 stress. Proc Natl Acad Sci U S A. 2023;120(11).
998 51. Coyte KZ, Tabuteau H, Gaffney EA, Foster KR, Durham WM. Microbial competition in porous
999 environments can select against rapid biofilm growth. Proc Natl Acad Sci U S A. 2017;114(2):E161-
1000 E70.
1001 52. Woo AC, Faure L, Dapa T, Matic I. Heterogeneity of spontaneous DNA replication errors in
1002 single isogenic *Escherichia coli* cells. Sci Adv. 2018;4(6):eaat1608.
1003 53. Fowler RG, Erickson JA, Isbell RJ. Activity of the *Escherichia coli mutT* mutator allele in an
1004 anaerobic environment. J Bacteriol. 1994;176(24):7727-9.
1005 54. Sakai A, Nakanishi M, Yoshiyama K, Maki H. Impact of reactive oxygen species on
1006 spontaneous mutagenesis in *Escherichia coli*. Genes to Cells. 2006;11(7):767-78.
1007 55. Shewaramani S, Finn TJ, Leahy SC, Kassen R, Rainey PB, Moon CD. Anaerobically Grown
1008 *Escherichia coli* Has an Enhanced Mutation Rate and Distinct Mutational Spectra. PLoS Genet.
1009 2017;13(1):e1006570.
1010 56. Becket E, Tse L, Yung M, Cosico A, Miller JH. Polynucleotide Phosphorylase Plays an
1011 Important Role in the Generation of Spontaneous Mutations in *Escherichia coli*. J Bacteriol.
1012 2012;194(20):5613-20.
1013 57. Garibyan L, Huang T, Kim M, Wolff E, Nguyen A, Nguyen T, et al. Use of the *rpoB* gene to
1014 determine the specificity of base substitution mutations on the *Escherichia coli* chromosome. DNA
1015 Repair (Amst). 2003;2(5):593-608.
1016 58. Yamagishi J, Yoshida H, Yamayoshi M, Nakamura S. Nalidixic acid-resistant mutations of the
1017 *gyrB* gene of *Escherichia coli*. Mol Gen Genet. 1986;204(3):367-73.
1018 59. Hall AR, Griffiths VF, Maclean RC, Colegrave N. Mutational neighbourhood and mutation
1019 supply rate constrain adaptation in *Pseudomonas aeruginosa*. Proc R Soc B Biol Sci.
1020 2010;277(1681):643-50.
1021 60. Arjan JA, Visser M, Zeyl CW, Gerrish PJ, Blanchard JL, Lenski RE. Diminishing returns from
1022 mutation supply rate in asexual populations. Science. 1999;283(5400):404-6.
1023 61. Sprouffske K, Aguilar-Rodriguez J, Sniegowski P, Wagner A. High mutation rates limit
1024 evolutionary adaptation in *Escherichia coli*. PLoS Genet. 2018;14(4):e1007324.
1025 62. Sane M, Diwan GD, Bhat BA, Wahl LM, Agashe D. Shifts in mutation spectra enhance access
1026 to beneficial mutations. Proc Natl Acad Sci U S A. 2023;120(22):e2207355120.

63. Cano AV, Rozhoňová H, Stoltzfus A, McCandlish DM, Payne JL. Mutation bias shapes the spectrum of adaptive substitutions. Proc Natl Acad Sci U S A. 2022;119(7):e2119720119.
64. Agashe D, Sane M, Singhal S. Revisiting the role of genetic variation in adaptation. The American Naturalist. 2023.
65. Javaux EJ. Challenges in evidencing the earliest traces of life. Nature. 2019;572(7770):451-60.
66. Imlay JA. Cellular Defenses against Superoxide and Hydrogen Peroxide. Annual Review of Biochemistry. 2008;77(1):755-76.
67. Melaugh G, Martinez VA, Baker P, Hill PJ, Howell PL, Wozniak DJ, et al. Distinct types of multicellular aggregates in Pseudomonas aeruginosa liquid cultures. npj Biofilms and Microbiomes. 2023;9(1):52.
68. Bergeron LA, Besenbacher S, Zheng J, Li P, Bertelsen MF, Quintard B, et al. Evolution of the germline mutation rate across vertebrates. Nature. 2023;615(7951):285-91.
69. Sung W, Ackerman MS, Miller SF, Doak TG, Lynch M. Drift-barrier hypothesis and mutation-rate evolution. Proc Natl Acad Sci U S A. 2012;109(45):18488-92.
70. Lynch M, Ackerman MS, Gout JF, Long H, Sung W, Thomas WK, et al. Genetic drift, selection and the evolution of the mutation rate. Nat Rev Genet. 2016;17(11):704-14.
71. Khademian M, Imlay JA. How Microbes Evolved to Tolerate Oxygen. Trends Microbiol. 2021;29(5):428-40.
72. Kubitschek HE, Friske JA. Determination of bacterial cell volume with the Coulter Counter. J Bacteriol. 1986;168(3):1466-7.
73. Sekiguchi M, Tsuzuki T. Oxidative nucleotide damage: consequences and prevention. Oncogene. 2002;21(58):8895-904.
74. R Core Team. R: A Language and Environment for Statistical Computing. 4.3.1 ed. Vienna, Austria: R Foundation for Statistical Computing; 2023.
75. Soetaert K, Petzoldt T, Setzer RW. Solving Differential Equations in R: Package deSolve. Journal of Statistical Software. 2010;33(1):1-25.
76. Bolker BM. Ecological models and data in R: Princeton University Press; 2008.
77. Wickham H, Averick M, Bryan J, Chang W, McGowan LDA, François R, et al. Welcome to the Tidyverse. Journal of Open Source Software. 2019;4(43):1686.
78. Pinheiro J, Bates D. Mixed-Effects Models in S and S-PLUS. Springer, New York.2000.
79. Lüdecke D. ggeffects: Tidy data frames of marginal effects from regression models. Journal of Open Source Software. 2018;3(26):772.
80. Dykhuizen D. Selection for Tryptophan Auxotrophs of *Escherichia coli* in Glucose-Limited Chemostats as a Test of the Energy Conservation Hypothesis of Evolution. Evolution. 1978;32(1):125-50.
81. Jain R, Srivastava R. Metabolic investigation of host/pathogen interaction using MS2-infected *Escherichia coli*. BMC Systems Biology. 2009;3(1):121.
82. Buckstein MH, He J, Rubin H. Characterization of Nucleotide Pools as a Function of Physiological State in *Escherichia coli*. J Bacteriol. 2008;190(2):718-26.
83. Bipatnath M, Dennis PP, Bremer H. Initiation and velocity of chromosome replication in *Escherichia coli* B/r and K-12. J Bacteriol. 1998;180(2):265-73.
84. Xia Z, Azurmendi HF, Mildvan AS. Transient State Kinetic Studies of the MutT-Catalyzed Nucleoside Triphosphate Pyrophosphohydrolase Reaction. Biochemistry. 2005;44(46):15334-44.
85. Lu AL, Yuen DS, Cillo J. Catalytic mechanism and DNA substrate recognition of *Escherichia coli* MutY protein. J Biol Chem. 1996;271(39):24138-43.
86. Kang M, Kim K, Choe D, Cho S, Kim SC, Palsson B, et al. Inactivation of a Mismatch-Repair System Diversifies Genotypic Landscape of *Escherichia coli* During Adaptive Laboratory Evolution. Front Microbiol. 2019;10:1845.
87. González-Flecha B, Demple B. Homeostatic regulation of intracellular hydrogen peroxide concentration in aerobically growing *Escherichia coli*. J Bacteriol. 1997;179(2):382-8.

88. Rodríguez-Rojas A, Makarova O, Müller U, Rolff J. Cationic Peptides Facilitate Iron-induced Mutagenesis in Bacteria. PLOS Genetics. 2015;11(10):e1005546.
89. Baba T, Ara T, Hasegawa M, Takai Y, Okumura Y, Baba M, et al. Construction of *Escherichia coli* K-12 in-frame, single-gene knockout mutants: the Keio collection. Molecular Systems Biology. 2006;2:2006.0008.
90. Deatherage DE, Barrick JE. Identification of mutations in laboratory-evolved microbes from next-generation sequencing data using breseq. Methods Mol Biol. 2014;1151:165-88.
91. Barrick JE, Colburn G, Deatherage DE, Traverse CC, Strand MD, Borges JJ, et al. Identifying structural variation in haploid microbial genomes from short-read resequencing data using breseq. BMC Genomics. 2014;15(1):1039.
92. Blattner FR, Plunkett G, 3rd, Bloch CA, Perna NT, Burland V, Riley M, et al. The complete genome sequence of *Escherichia coli* K-12. Science. 1997;277(5331):1453-62.
93. Grenier F, Matteau D, Baby V, Rodrigue S. Complete Genome Sequence of *Escherichia coli* BW25113. Genome Announc. 2014;2(5).
94. Krasovec R, Richards H, Gomez G, Gifford DR, Mazoyer A, Knight CG. Measuring Microbial Mutation Rates with the Fluctuation Assay. J Vis Exp. 2019(153).
95. Rosche WA, Foster PL. Determining mutation rates in bacterial populations. Methods. 2000;20(1):4-17.
96. Luria SE, Delbrück M. Mutations of Bacteria from Virus Sensitivity to Virus Resistance. Genetics. 1943;28(6):491-511.
97. Fox J, Weisberg S. An R companion to applied regression: Sage publications; 2018.
98. Stewart FM. Fluctuation Tests: How Reliable Are the Estimates of Mutation Rates? Genetics. 1994;137(4):1139-46.

Supporting Information

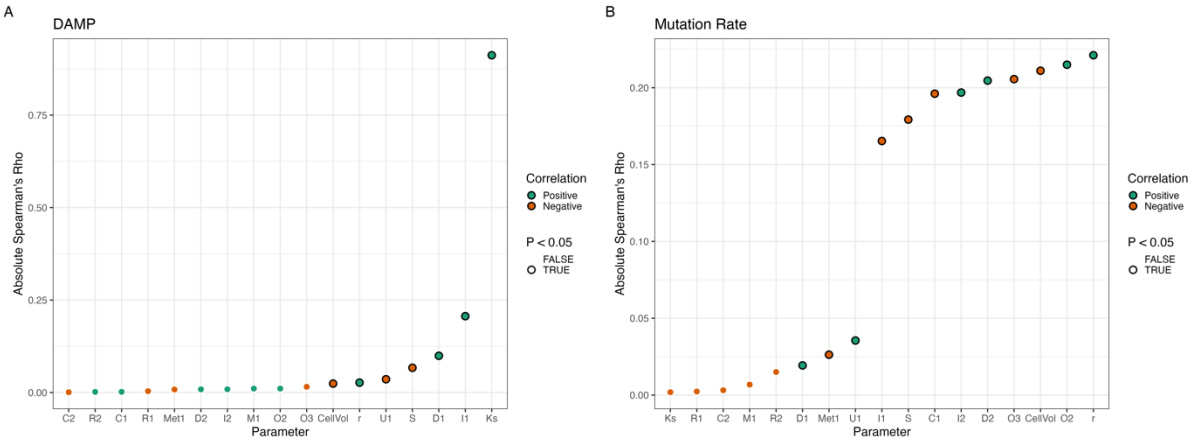

Figure S1. ***Global Sensitivity Analysis of Model A:*** *Left Hand Side (A) shows the rank correlation, as quantified by Spearman's Rank Correlation Coefficient, between each parameter and the slope of DAMP, parameters are ordered from least to most correlation from left to right. Right Hand Side (B) shows the equivalent information for the correlation between parameter values and mutation rate (at 250 mg L^{-1}). Positive correlations are shown in green whilst negatively correlated parameters are shown in orange. Black borders show significant rank correlation ($P < 0.05$). Note the different y axis limits and x axis order on the left VS right hand side.*

1112

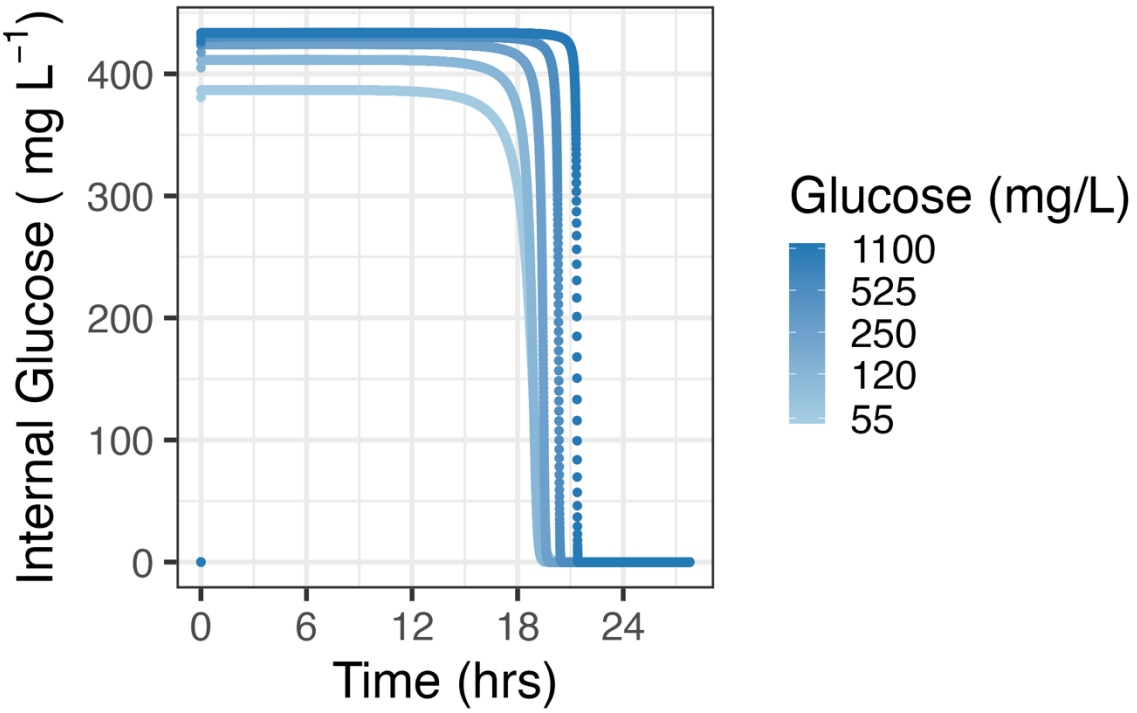

1113 *Figure S2**. Dynamics of internal glucose over time** in model A simulated at 5 log-spaced glucose concentrations*
1114 *from 55 to 1100 mg L^{-1}. Higher levels of initial external glucose provision (point colour) lead to higher levels of internal*
1115 *glucose (y-axis).*

1116

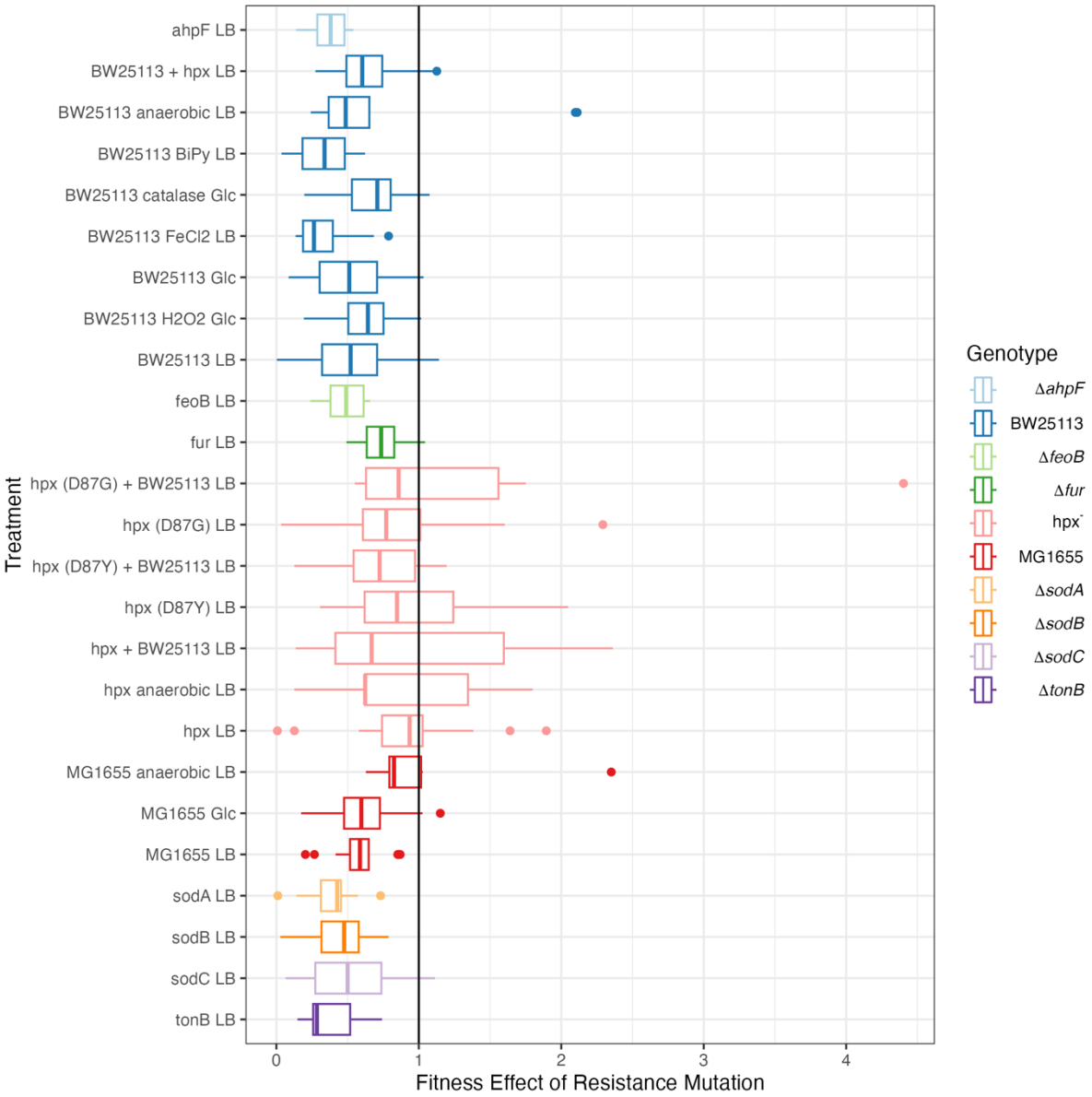

1117 *Figure S3.* ***Fitness effects of resistance mutations*** *where fitness is coestimated with mutational events. Boxplots*
1118 *shown for each treatment with colour representing genotype. Vertical lines inside boxes represent the median for that*
1119 *treatment, with the boxes depicting the interquartile range. The black vertical line at a fitness effect size of 1 represents*
1120 *neutral fitness effects.*

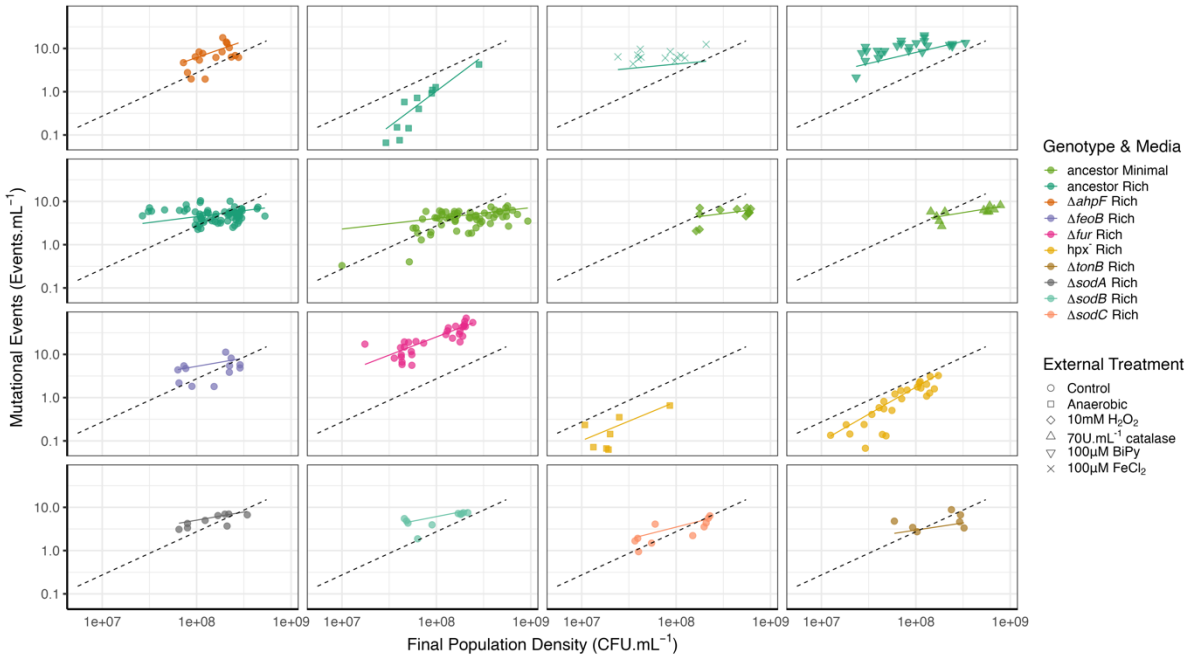

*Figure S4. **Raw data used in figure 3**: Final population density is plotted against mutational events per mL on a log-log scale. Dashed lines show the null expectation of a constant mutation rate (i.e. slope=1) y intercept for dashed line is arbitrary. Coloured lines are fitted slopes from mod3 (Supplementary Statistics file), line gradients with 95% CI shown in figure 3. Treatments shown are BW25113 ancestor (1106 parallel cultures (pc) across 69 fluctuation assays (fa)); ancestor minimal media (942 pc, 59 fa); ΔahpF (266 pc, 17 fa); hpx⁻ (402 pc, 26 fa); ancestor anaerobic (168 pc, 11 fa); ancestor 10mM H_2O_2 (179 pc, 12 fa); ancestor 70U mL^{-1} catalase (167 pc, 11 fa); hpx⁻ anaerobic (105 pc, 7 fa); ancestor + chelator 2,2,Bipyridyl 100μM (382 pc, 24 fa); ancestor + $FeCl_2$ 100μM (210 pc, 13 fa); ΔfeoB (192 pc, 12 fa); Δfur (504 pc, 31 fa); ΔtonB (113 pc, 7 fa).*

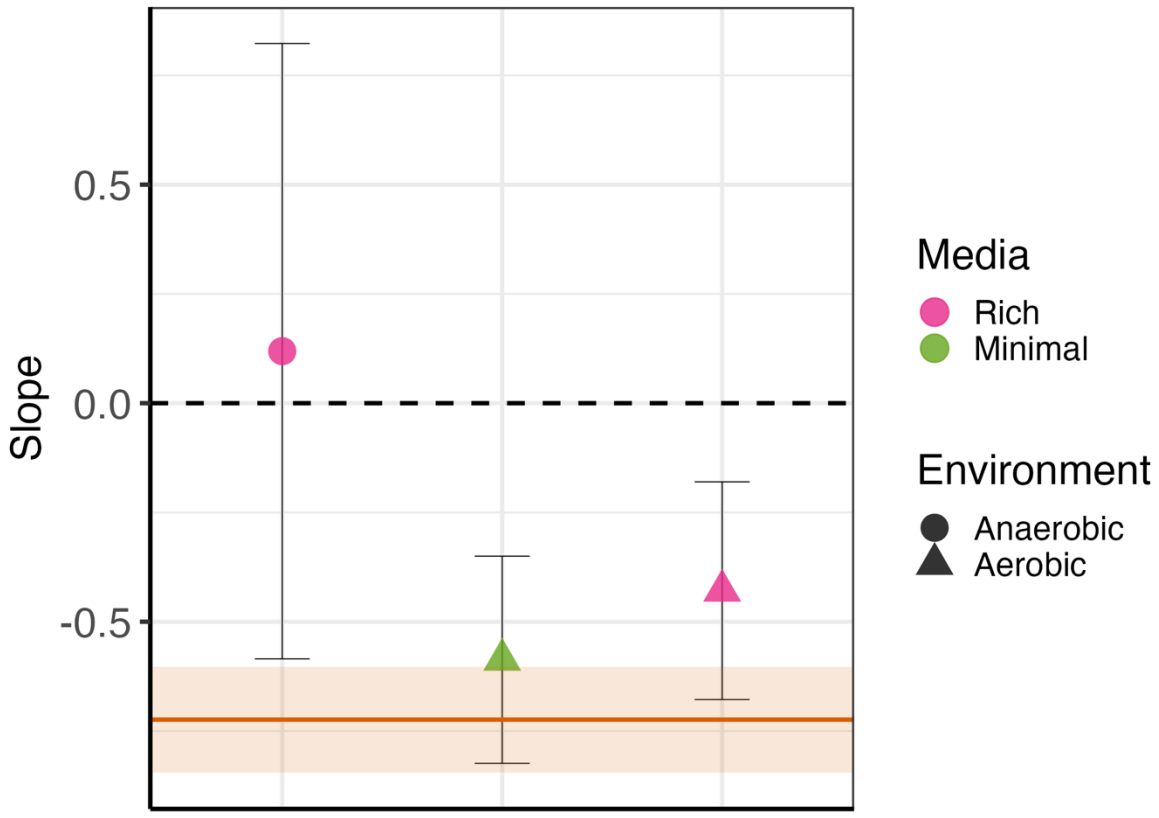

Figure S5. ***log-log relationship between population density (CFU mL^{-1}) and mutational events (mL^{-1}) in wild-type strain MG1655 under aerobic and anaerobic conditions.*** *Pink circle = MG1655 rich media anaerobic (173 pc, 11 fa); Green triangle = MG1655 minimal media aerobic (273 pc, 17 fa); Pink Triangle = MG1655 rich media aerobic (285 pc, 18 fa). Orange line and shaded area shows DAMP for BW25113 in rich media as in Fig. 3 with 95% CI.*

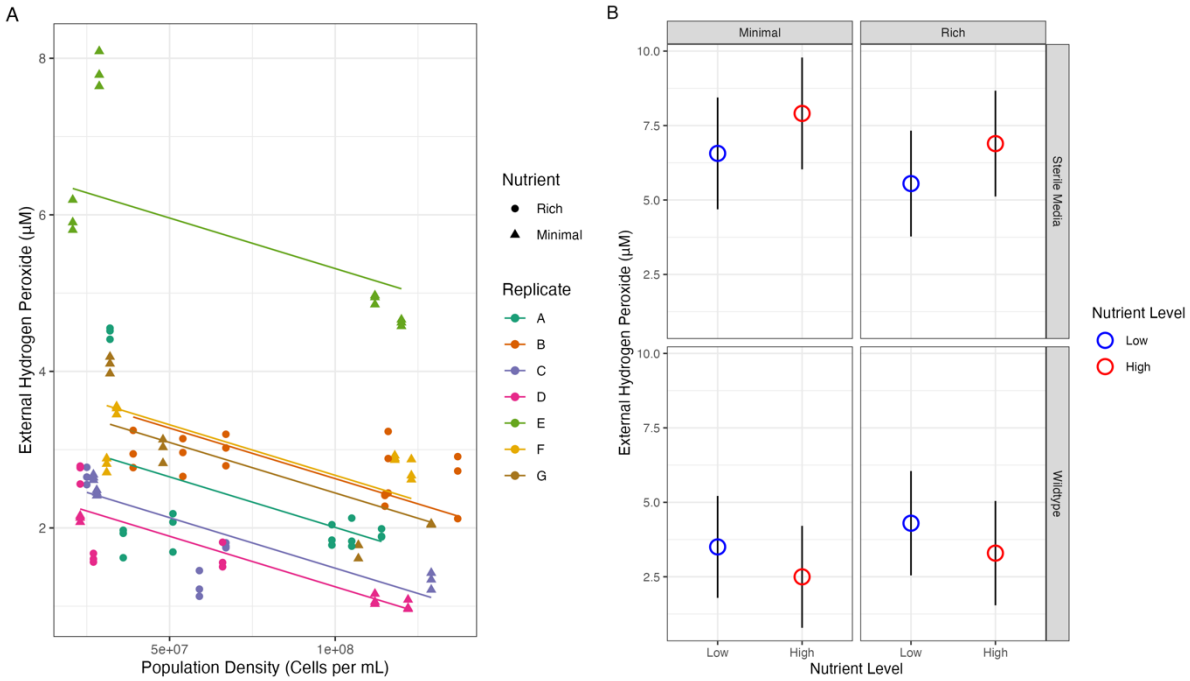

Figure S6. ***Effects of Population Density and Nutrient Level on H_2O_2*** *Left Hand Side (A) shows the relationship between population density and external H_2O_2 in cultures of MG1655 after 24 hours of incubation. Rich media is 2/5% LB diluted in DM, minimal media is 80/1000 mg L^{-1} glucose in DM. Population density is estimated from the optical density given the assumption that OD 1 = 1 x 10^9 cells mL^{-1}. Lines are from regression 7B (SI). Right Hand Side (B) shows the H_2O_2 concentration after 24 hours incubation in rich or minimal media; sterile or with wild-type MG1655, Regression 6 (SI); error bars show 95% CI. The interaction effect between nutrient level (Low versus High) and presence of a culture (Sterile Media versus Wild-type), where external peroxide decreases with nutrients increases in the presence of a culture but increases without one, is highly significant ($F_{DF=46}$ = 9.8, P = 3x10^{-3}, Regression 6 (SI)).*

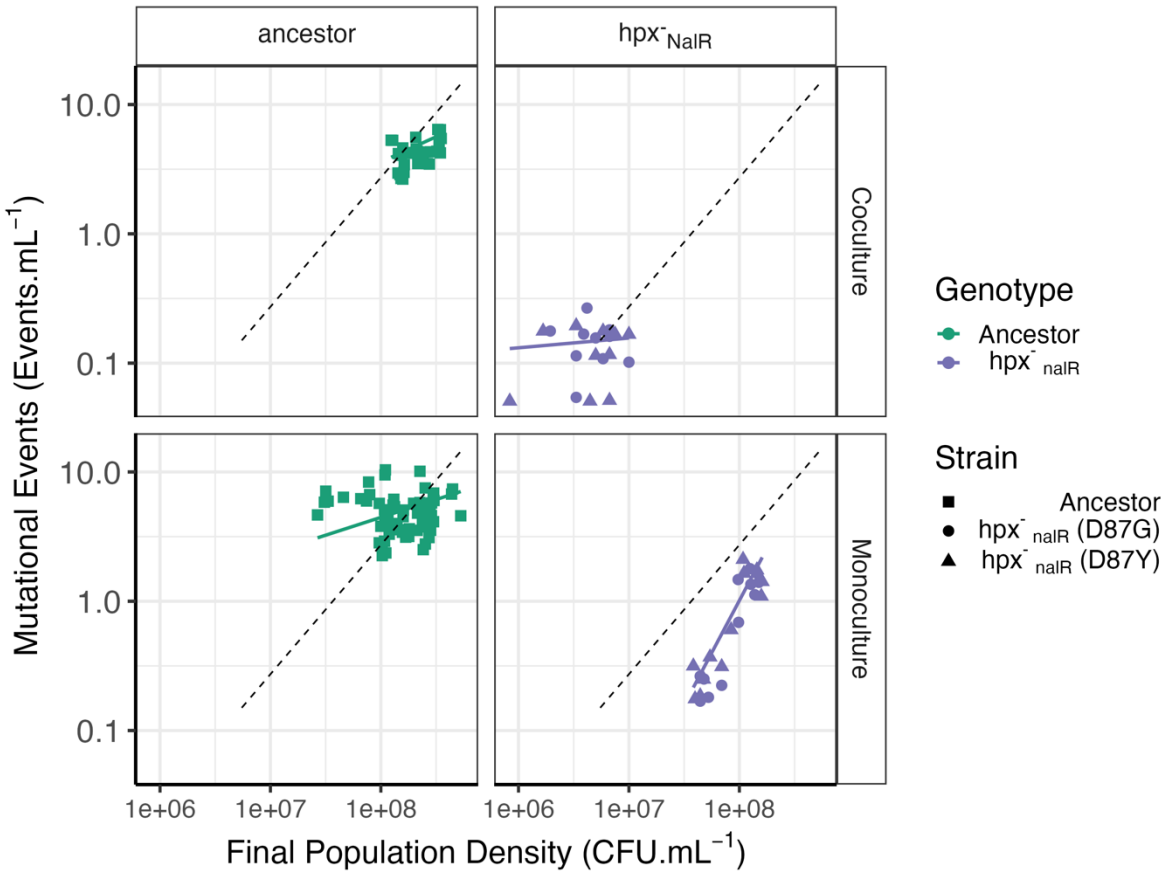

*Figure S7. **Raw data used in figure 4**: Final population density of the focal strain is plotted against mutational events per mL on a log-log scale. Dashed lines show the null expectation of a constant mutation rate with a slope of 1. Ancestor coculture measurements are taken in coculture with hpx-, hpx D87Y & D87G are cocultured with ancestor BW25113. Lines are fitted slopes shown in fig. 4. BW25113 ancestor (1106 pc, 69 fa); BW25113 in coculture with hpx- (498 pc, 31 fa); hpx- nalR (388 pc, 24 fa); hpx- nalR in coculture with BW25113 (319 pc, 20 fa).*

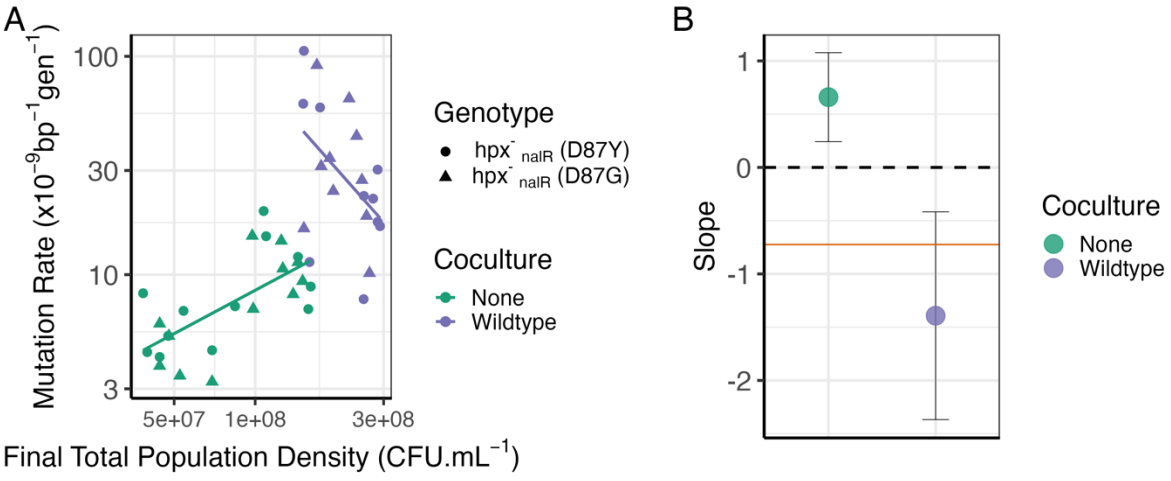

*Figure S8. **Relationship between total population density and mutation rate in hpx- with cocultured wild-type BW25113**. A: Final population density (focal + coculture strain where relevant) is plotted against mutation rate on a log-log scale. hpx- nalR monoculture (388 pc, 24 fa); hpx- nalR in coculture with BW25113 (319 pc, 20 fa). Lines are fitted slopes shown from Regression 8 (SI). B: Slope and 95% CI on the lines shown in LHS graph. Horizontal orange line shows the slope of the BW25113 ancestor in rich media (Regression 4 (SI), Fig. 3). In monoculture hpx- mutation rates increase with total population density whilst in coculture the wild-type restores a negative association between density and mutation rates (DAMP).*

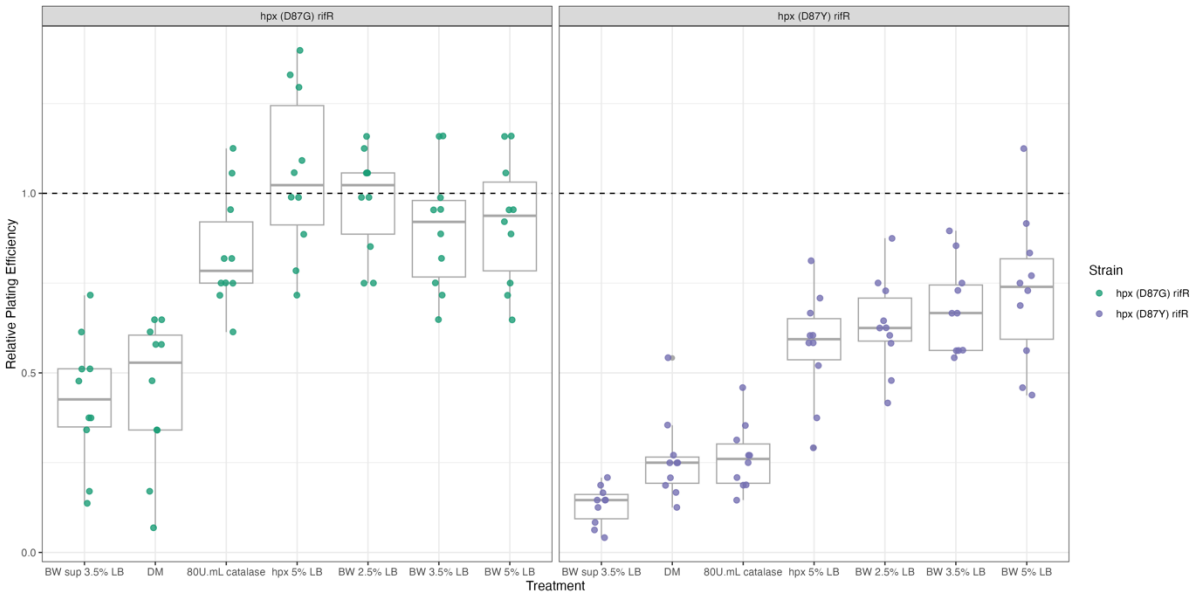

*Figure S9. **Reconstruction test showing the plating efficiency of rifampicin resistant hpx⁻ (D87Y) and hpx⁻ (D87G)** when combined and plated in 1.25mL with: supernatant from mid-density BW25113, sterile DM media, DM media with 800U mL^{-1} catalase, hpx⁻ low-density, BW25113 low-density, BW25113 mid-density, BW25113 high-density. Plating efficiency is calculated as the number of colonies counted divided by the number of colonies counted on non-selective TA agar plates without any additional treatment.*

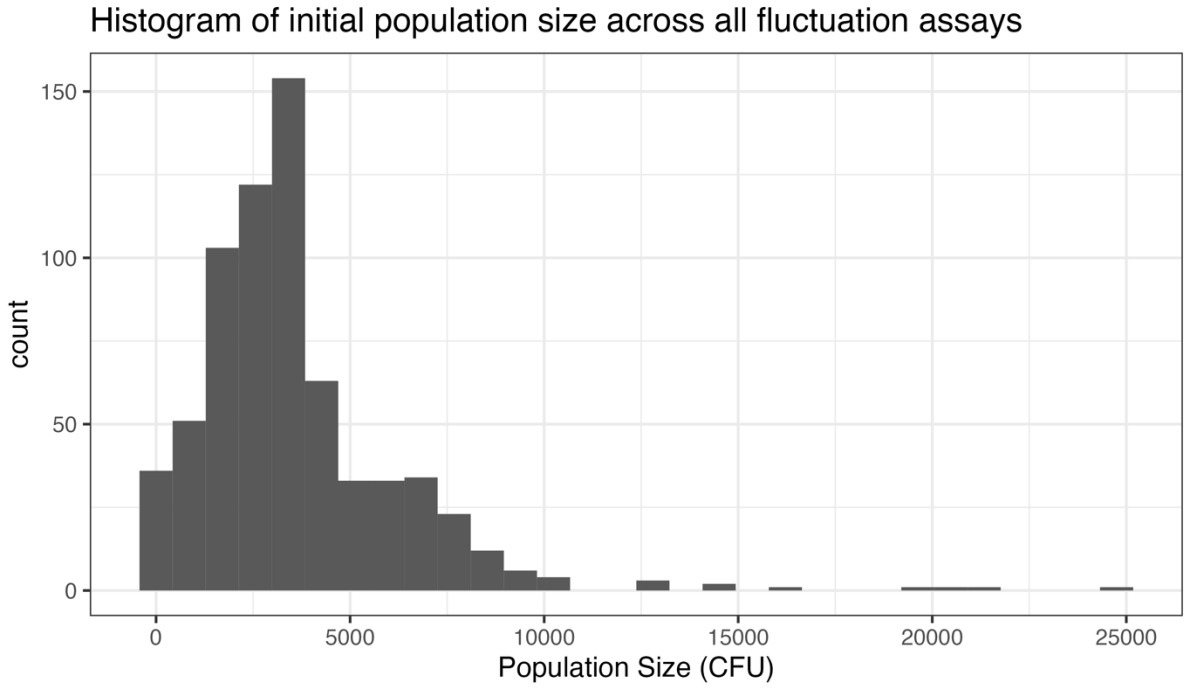

*Figure S10. **Distribution of initial population size across all fluctuation assays.** Mean = 3397, median = 3000. Low population size is desirable in order to reduce the chances of resistant mutants being present in the starting population ('jackpot cultures').*

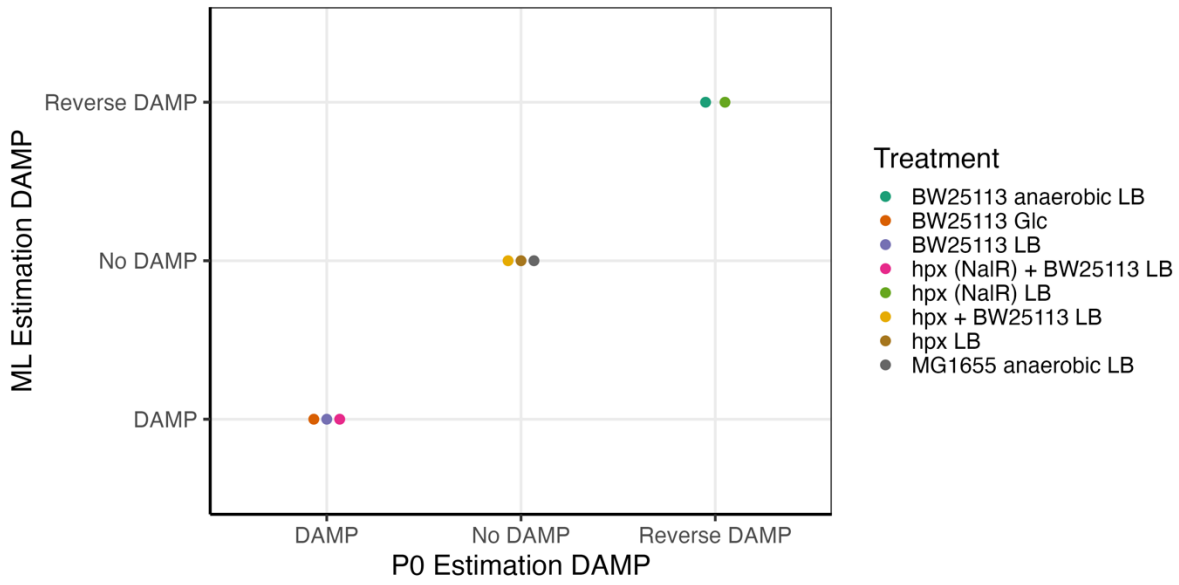

Figure S11. ***DAMP is seen in the same set of treatments using Maximum Likelihood or p_0 estimation methods.*** *Treatments in which 8< fluctuation assays can be analysed by the p_0 method are shown. Colour indicates treatment identity. Treatments without DAMP in both methods (No DAMP:No DAMP) are: hpx^- + BW25113, hpx^- and MG1655 anaerobic. Treatments with DAMP in both methods (DAMP:DAMP) are: BW25113 glucose, BW25113 LB and hpx^-_{nalR} + BW25113. Treatments with reverse DAMP (a significantly positive association between mutation rate and population density; Reverse DAMP:Reverse DAMP) are BW25113 anaerobic LB and hpx^-_{nalR} LB. No treatments show a change in conclusions between methods.*

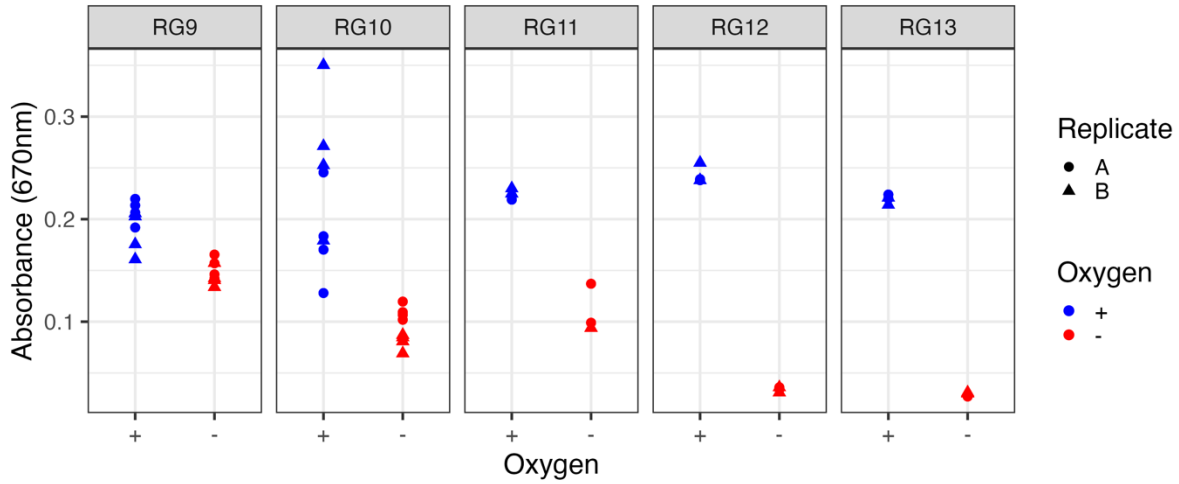

Figure S12. ***Reduction of resorufin to dihydro resorufin by anaerobic respiration*** *results in reductions in absorbance at 670nm verifying the anaerobic conditions during anaerobic fluctuation assays. Each of 5 blocks is shown as a separate facet; within each block 2 sets of paired fluctuation assays (A&B) were conducted in aerobic and anaerobic conditions, for each of these sets 2-4 measurements of resorufin/dihydro resorufin absorbance were taken after 24 hours of growth.*

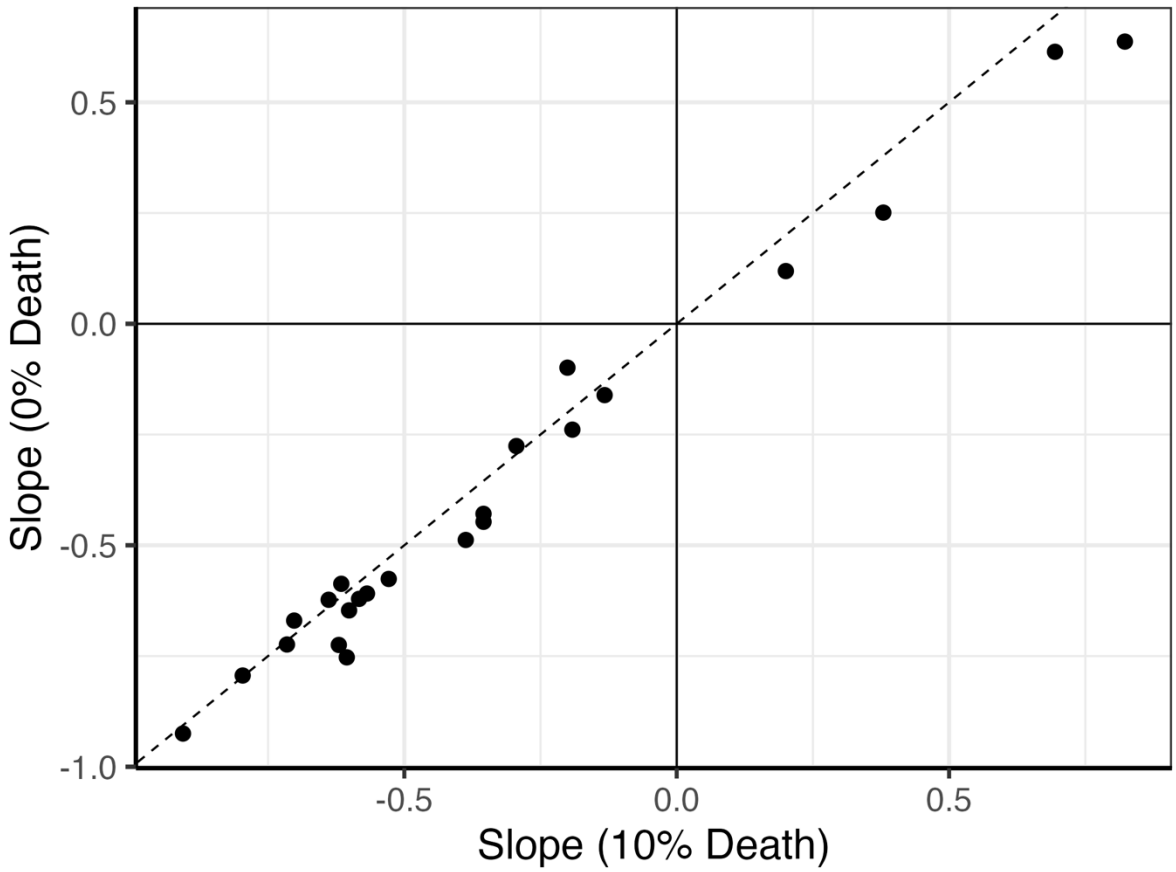

Figure S13. ***An assumption of 10% death has little effect on the estimation of DAMP slope.*** *Solid lines indicate a slope of 0 (no DAMP), dashed line shows identical slope values for both estimates. All treatments remain in the same category (DAMP, no DAMP or reverse DAMP).*

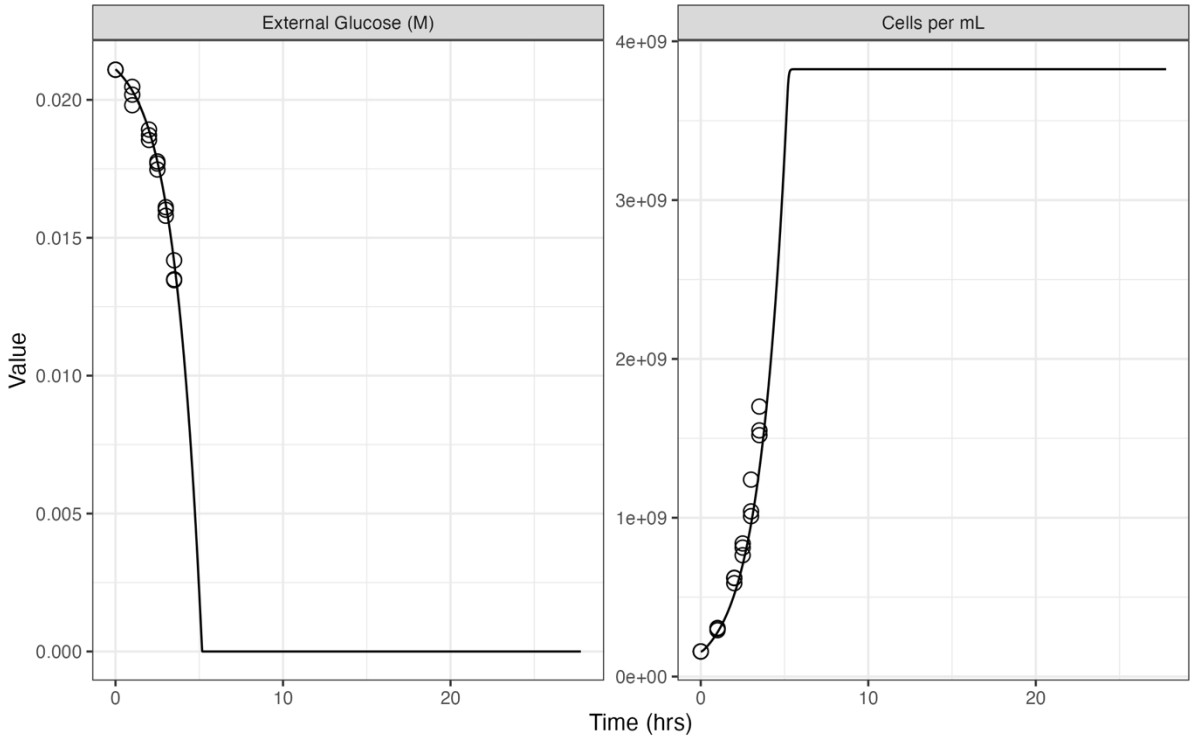

Figure S14. ***Fit of model variant A to published data.*** *Lines show results of ODE model A and circles show data from (81) used to fit parameters U1 and M1. Left-hand panel shows the molar concentration of external glucose over time and right-hand panel shows E. coli cells per mL over time.*

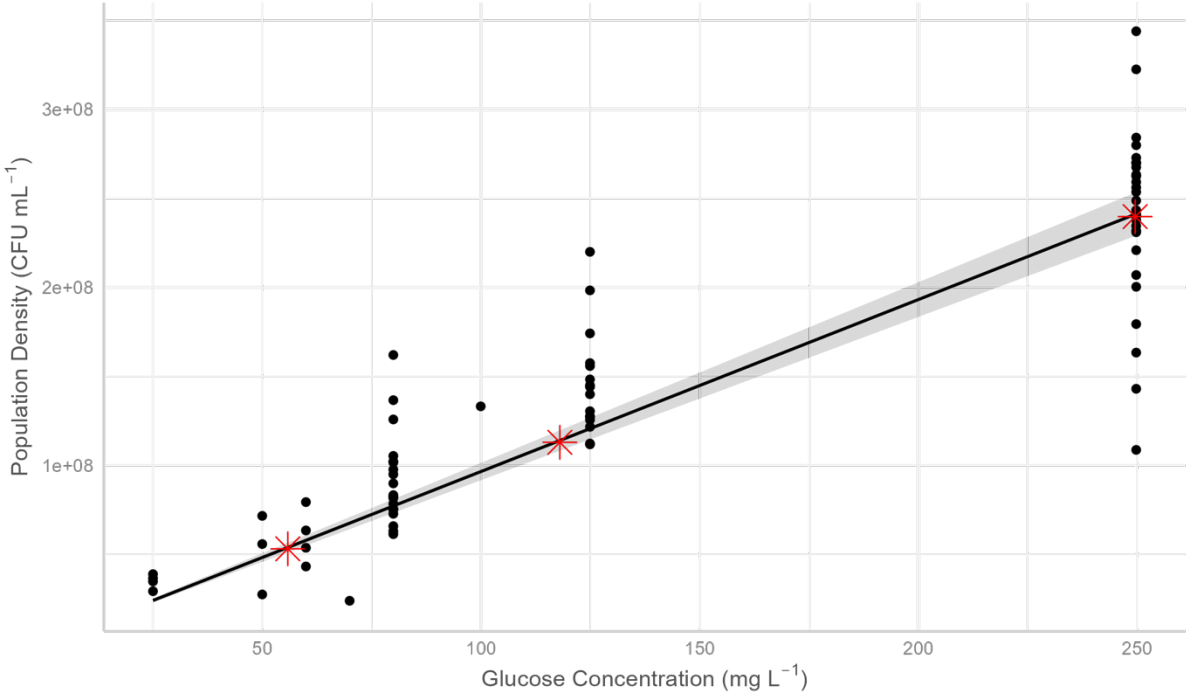

Figure S15. ***Fit of linear mixed effects model relating final population density to initial glucose concentration.*** *Used to fit parameter Met1 in ODE models. Black points show published lab data from (3) on population density and glucose provision in E. coli MG1655 used to fit this regression. Black line and shaded area show fitted relationship and 95% confidence interval respectively of a mixed effects model accounting for random effects of experimental block and plate. Red stars show output, in final population density, from initial ODE model A under differing initial glucose concentrations.*

Treatment	Slope	Slope_CI95	pValue	ChiSq	FA	PC	Plasticity
ahpF LB	-0.239	0.435	0.281	1.16	17	266	Constant
BW25113 + hpx LB	-0.609	0.291	4.03E-05	16.9	31	498	DAMP
BW25113 anaerobic LB	0.637	0.414	0.00256	9.1	11	168	Reverse DAMP
BW25113 FeCl2 LB	-0.794	0.212	2.36E-13	53.7	13	210	DAMP
BW25113 BiPy LB	-0.488	0.133	6.39E-13	51.7	24	382	DAMP
BW25113 LB	-0.724	0.121	8.17E-32	138	69	1106	DAMP
BW25113 Glc	-0.753	0.109	1.02E-41	183	59	942	DAMP
BW25113 H2O2 Glc	-0.725	0.283	4.98E-07	25.3	12	179	DAMP
BW25113 catalase Glc	-0.647	0.234	5.97E-08	29.4	11	167	DAMP
feoB LB	-0.621	0.381	0.00138	10.2	12	192	DAMP
fur LB	-0.161	0.162	0.0512	3.8	31	504	Constant
hpx + BW25113 LB	-0.276	0.493	0.272	1.2	13	207	Constant
hpx anaerobic LB	-0.0991	0.61	0.75	0.101	7	105	Constant
hpx LB	0.251	0.262	0.0603	3.53	26	402	Constant
hpx (NalR) + BW25113 LB	-0.925	0.535	7.04E-04	11.5	20	319	DAMP
hpx (NalR) LB	0.614	0.381	0.00159	9.97	24	388	Reverse DAMP
MG1655 anaerobic LB	0.119	0.704	0.74	0.11	11	173	Constant
MG1655 LB	-0.429	0.249	7.31E-04	11.4	18	285	DAMP
MG1655 Glc	-0.587	0.237	1.22E-06	23.5	17	273	DAMP

sodA LB	-0.623	0.233	1.55E-07	27.5	9	134	DAMP
sodB LB	-0.576	0.233	1.32E-06	23.4	10	151	DAMP
sodC LB	-0.447	0.342	0.0103	6.58	10	150	DAMP
tonB LB	-0.67	0.299	1.14E-05	19.3	7	113	DAMP

Table S1: Slope estimates with associated Chi-Squared tests from Regression 4 (SI). *Slope indicates the log-log relationship between population density and mutational events per mL minus 1 (1 is subtracted to make interpretation simpler as a constant mutation rate is now defined by a slope of 0 rather than a slope of 1). Slope_CI95 indicates that a 95% confidence interval on the slope estimate will be slope ± slope_CI95. pValue is calculated from a Chi-Squared test (DF=1) comparing the original slope value to the Null Hypothesis that the slope of the given treatment = 1 (slope = 1 when mutation rate is constant with respect to population density); therefore in treatments in which the slope significantly differs from 1 we have observed density associated mutation rate plasticity. FA and PC list the number of fluctuation assays and parallel cultures used in the analysis respectively. Plasticity shows if the treatment shows a constant mutation rate, DAMP (a significant inverse relationship between population density and mutation rate) or reverse DAMP (a significant direct relationship between population density and mutation rate).*

Genotype	Mutations	Missing Coverage
***ahpF* knockout (BW25113)**	(gene: *lrhA* ←, position: 2399603, mutation: C to T, annotation: W173* (TGG→TAG))	(gene: *ahpF*, position: 635078-636851)
***feoB* knockout (BW25113)**	(gene: *lrhA* ← / → *alaA* intergenic, position = 2400193, mutation: IS2 (+) +5bp, annotation: intergenic (-73/-843)) (gene: *fimE* →, position = 2,400,193, mutation = IS1 (–) +9 bp, annotation = coding (12-20/597 nt))	(gene: *feoA-feoB-feoC,* position: 3533735-3536122)
***fur* knockout (BW25113)**	(gene: *ynjI* ← / ← *topB* intergenic, position: 1,839,184, mutation: $(A)_8$→$(A)_7$, annotation: intergenic (-56/+72)) (gene: *kgtP* ← / ← *rrfG,* position: 2,719,426, mutation: T→C, annotation: intergenic (-321/+2)) (gene: *ytfT* →, position: 4,442,904, mutation: G→A, annotation: G173R (GGA→AGA))	(gene: *fur-uof,* position: 705581-706177)
hpx⁻ (MG1655)	(gene: *insB9–[crl],* position: 257,908, mutation: Δ776 bp) (gene: *ybiT* → / ← *ybiU,* position: 857,609, mutation: C→A, annotation: intergenic (+54/+187)) (gene: *ymfE* ← / → *lit,* position: 1,198,505, mutation: $(AATGATGA)_6$→ $(AATGATGA)_7$, annotation: intergenic (-268/-190)) (gene: *insH21*, position: 1,299,499, mutation: Δ1,199 bp) (gene: *insB5–insA5,* position: 1,978,503, mutation: Δ776 bp) (gene: *gatD* ← / ← *gatB,* position: 2,173,363, mutation: Δ2 bp, annotation: intergenic (-490/+918))	(gene: *ahpC-ahpF*, position: 638661-641020) (gene: *rrlD,* position: 3423791-3424238) (gene: *fecD*, position: 4511728-4511917)

	(gene: *rtcR* → / ← *glpG,* position: 3,560,455, mutation: +G, annotation: intergenic (+589/+167)) (gene: *frwC* →, position: 4,143,377, mutation: C→T, annotation: S283L (TCA→TTA)) (gene: *gltP* → / ← *yjcO,* position: 4,296,381, mutation: +GC, annotation: intergenic (+587/+55))	
hpx⁻$_{nalR}$ (D87Y) (MG1655)	(gene: *rrfH* →, position: 228,796, mutation: G→A, annotation: noncoding (41/120 nt)) (gene*: insB9–[crl],* position: 257,908, mutation: Δ776 bp) (gene: *ybiT* → / ← *ybiU*, position: 857,609, mutation: C→A, annotation: intergenic (+54/+187)) (gene: *insH21*, position: 1,299,499, mutation: Δ1,199 bp) (gene: *azoR* ←, position: 1,482,580, mutation: G→A, annotation: A94V (GCA→GTA)) (gene: *motB* ←, position: 1,976,012, mutation: G→A, annotation: P82S (CCA→TCA)) (gene:*insB5–insA5,* position: 1,978,503, mutation: Δ776 bp) (gene: *gatD* ← / ← *gatB*, position: 2,173,363, mutation: Δ2 bp, annotation: intergenic (-490/+918)) (gene: *gyrA* ←, position: 2,339,162, mutation: C→A, annotation: D87Y (GAC→TAC)) (gene: *ygdQ* →, position: 2,970,579, mutation: Δ1 bp, annotation: coding (160/714 nt)) (gene: *rtcR* → / ← *glpG*, position: 3,560,455, mutation: +G, annotation: intergenic (+589/+167)) (gene: *frwC* →, position: 4,143,377, mutation: C→T, annotation: S283L (TCA→TTA)) (gene: *gltP* → / ← *yjcO*, position: 4,296,381, mutation: +GC, annotation: intergenic (+587/+55))	(gene: *ahpC-ahpF*, position: 638630-641000) (gene*:rrlD*, position: 3423717-3424239)

hpx⁻ nalR (D87G) (MG1655)	(gene: insB9–[crl], position: 257,908, mutation: Δ776 bp) (gene: ybiT → / ← ybiU, position: 857,609, mutation: C→A, annotation: intergenic (+54/+187)) (gene: ymfE ← / → lit, position: 1,198,505, mutation: $(AATGATGA)_6$→ $(AATGATGA)_7$, annotation: intergenic (-268/-190)) (gene: insH21, position: 1,299,499, mutation: Δ1,199 bp) (gene: insB5–insA5, position: 1,978,503, mutation: Δ776 bp) (gene: gatD ← / ← gatB, position: 2,173,363, mutation: Δ2 bp, annotation: intergenic (-490/+918)) (gene: gyrA ←, position: 2,339,162, mutation: T→C, annotation: D87G (GAC→GGC)) (gene: rtcR → / ← glpG, position: 3,560,455, mutation: +G, annotation: intergenic (+589/+167)) (gene: waaU ←, position: 3,799,310, mutation: C→A, annotation: M1M (ATG→ATT)) (gene: frwC →, position: 4,143,377, mutation: C→T, annotation: S283L (TCA→TTA)) (gene: gltP → / ← yjcO, position: 4,296,381, mutation: +GC, annotation: intergenic (+587/+55))	(gene: *ahpC-ahpF*, position: 638651-641053) (gene:*rrlD*, position: 3423755-3424238)
***tonB* knockout (BW25113)**	(gene: *flhD* ← / → *uspC,* position: 1,972,749, mutation: IS5 (+) +3 bp :: +C, annotation: intergenic (-295/-483))	(gene: *tonB-yciA*, position: 1305230-1306150)

Table. S2: Mutations, missing coverage and new junction evidence for key strains in this study as predicted by variant calling with breseq.

Data Table Name	Column Name	Description
SupData1_Fluctuation Assays.csv	assay_ID	Unique identifier for the fluctuation assay
	block	Experimental block
	date	Date of assay start
	plate_ID	Experimental plate
	External_Treatment	Any additions made to the growth media
	genotype	Identifier for the focal strain genotype
	Selective_marker	Antibiotic used as a selective marker (rif for rifampicin; nal for nalidixic acid)
	stock	Identifier for the glycerol stock used

coculture_strain	Identifier for the genotype of a cocultured strain
coculture_ID	Identifier for the coculture giving the two strains in a fixed order
genotype2	Identifier for the coculture giving the focal strain first
Media	Basic growth media used (DM = Davis Minimal Media)
LB_perc	Percentage LB added to the media (i.e. 2% = 440 µL in 22mL)
GlcMedia	Was glucose used as the nutrient source (y for yes; n for no)
Mut_to_WT_ratio	Ratio of the volume of mutant cell culture to wild-type in the parallel cultures (i.e. in a 1.25mL culture if 1.24mL of mutant culture is added to 10µL wt culture the ratio will be 24)
glucose	The initial glucose concentration in mg per L
N0_ul	The volume of the initial culture plated to calculate the N0 (initial population size) in µL .
N0_CFU_nx	CFU on the N0 plate containing nalidixic acid
N0	Initial population size (N0_CFU multiplied by fluctuation_volume_t0 divided by the N0_ul)
N0_coculture	Initial population size of the coculture strain
N0_gen_to_co_ratio	N0 of the focal strain divided by the N0 of the coculture strain
Nt1_CFU_nx	CFU on the 1st Nt plate containing nalidixic acid
Nt2_CFU_nx	CFU on the 2nd Nt plate containing nalidixic acid
Nt3_CFU_nx	CFU on the 3rd Nt plate containing nalidixic acid
Nt1_CFU	CFU on the 1st Nt plate
Nt2_CFU	CFU on the 2nd Nt plate
Nt3_CFU	CFU on the 3rd Nt plate
N0_CFU	CFU on the N0 plate
Nt1_nx	Estimated final population size from Nt1_CFU_nx (Nt1_CFU_nx multiplied by Nt_dilution_nx multiplied by the final culture volume divided by 40µL (the Nt plating volume).
Nt2_nx	Estimated final population size from Nt2_CFU_nx (Nt2_CFU_nx multiplied by Nt_dilution_nx multiplied by the

	final culture volume divided by 40µL (the Nt plating volume).
Nt3_nx	Estimated final population size from Nt3_CFU_nx (Nt3_CFU_nx multiplied by Nt_dilution_nx multiplied by the final culture volume divided by 40µL (the Nt plating volume).
Nt1	Estimated final population size from Nt1_CFU (Nt1_CFU multiplied by Nt_dilution multiplied by the final culture volume divided by 40µL (the Nt plating volume).
Nt2	Estimated final population size from Nt2_CFU (Nt2_CFU multiplied by Nt_dilution multiplied by the final culture volume divided by 40µL (the Nt plating volume).
Nt3	Estimated final population size from Nt3_CFU (Nt3_CFU multiplied by Nt_dilution multiplied by the final culture volume divided by 40µL (the Nt plating volume).
environment	The glucose concentration of LB percentage used as nutrient source.
CI_range_coculture_strain	Upper bound of the estimated m for the coculture strain minus the lower bound of the m estimate for the coculture strain
CI_range_genotype	Upper bound of the estimated m for the focal strain minus the lower bound of the m estimate for the focal strain
fluctuation_volume_t0	Initial fluctuation assay volume for each parallel culture (in µL)
culture_volume_final	Final volume for each parallel culture calculated as fluctuation_volume_t0 minus the difference between initial and final weight of the plate divided by the 96 wells. This accounts for evaporation during the incubation.
coculture	Is this a coculture of two strains (y for yes; n for no)
D_gen_nx	The CFU density per mL as calculated from Nt plates containing nalidixic acid. The mean of the Nt_nx estimates multiplied and by the ratio of the plated volume (40µL) to the scaled volume (1000µL).
D_gen_all	The CFU per mL as calculated from Nt plates with and without nalidixic acid. The mean of the Nt_nx estimates and

	Nt estimates multiplied by the ratio of the plated volume (40µL) to the scaled volume (1000µL) (40/1000=25).
D_genotype	The CFU per mL as calculated from Nt plates not containing nalidixic acid. The mean of the Nt estimates multiplied by the ratio of the plated volume (40µL) to the scaled volume (1000µL).
D_coculture_strain	The density of the coculture strain in CFU per mL.
D_total	The total CFU density per mL (focal + coculture strain).
generations	The estimated number of generations as the log of the final population size minus the log of the initial population size all divided by the log of 2
generations_coculture_strain	Estimated generations of the coculture strain
incubation_mins	Incubation time for the fluctuation assay parallel cultures.
m_coculture_strain	Estimated average number of mutational events in each parallel culture of the coculture strain
m_genotype	Estimated average number of mutational events in each parallel culture of the focal strain
m_lower_genotype	Lower bound of 95% CI on the estimate of m
m_upper_genotype	Upper bound of 95% CI on the estimate of m
mut_fitness_genotype	Estimated fitness ratio of the wild-type strain to the mutants with rif or nal resistance.
FlanWarnings	Any warnings given by the 'flan' r package in estimating m
m_lower_coculture_strain	Lower bound of 95% CI on the estimate of m for the coculture strain
m_upper_coculture_strain	Upper bound of 95% CI on the estimate of m for the coculture strain
mutation_rate_coculture_strain	Mutation rate of the coculture strain calculated as the estimated m divided by Nt_genotype and then multiplied by $1x10^9$
mutation_rate_gen_all	Mutation rate of the coculture strain calculated as the estimated m divided by Nt_gen_all and then multiplied by $1x10^9$
mutation_rate_gen_allL	Lower bound of the mutation rate of the coculture strain calculated as the estimated lower bound of m divided

	by Nt_gen_all and then multiplied by $1x10^9$
mutation_rate_gen_allU	Upper bound of the mutation rate of the coculture strain calculated as the estimated upper bound of m divided by Nt_gen_all and then multiplied by $1x10^9$
mutation_rate_gen_nx	Mutation rate of the coculture strain calculated as the estimated m divided by Nt_gen_nx and then multiplied by $1x10^9$
mutation_rate_gen_nxL	Lower bound of the mutation rate of the coculture strain calculated as the estimated lower bound of m divided by Nt_gen_nx and then multiplied by $1x10^9$
mutation_rate_gen_nxU	Upper bound of the mutation rate of the coculture strain calculated as the estimated upper bound of m divided by Nt_gen_nx and then multiplied by $1x10^9$
mutation_rate_genotype	Mutation rate of the coculture strain calculated as the estimated m divided by Nt_genotype and then multiplied by $1x10^9$
mutation_rate_genotype_lower	Lower bound of the mutation rate of the coculture strain calculated as the estimated lower bound of m divided by Nt_genotype and then multiplied by $1x10^9$
mutation_rate_genotype_upper	Upper bound of the mutation rate of the coculture strain calculated as the estimated upper bound of m divided by Nt_genotype and then multiplied by $1x10^9$
Mutations_per_generation	m_genotype divided by generations
N_cultures	Number of parallel cultures plated on selective (rif or nal) agar
Nt_gen_all	The mean of Nt1,Nt2,Nt3,Nt_nx_1,Nt_nx_2,Nt_nx_3
Nt_gen_nx	The mean of Nt_nx_1,Nt_nx_2,Nt_nx_3
Nt_genotype	The mean of Nt1,Nt2,Nt3
Nt_coculture_strain	The estimated final population size for the coculture strain
Nt_CV	The coefficient of variability between Nt1, Nt2 and Nt3 (Standard deviation divided by mean value)

Nt_dilution_nx	Dilution factor for Nt plates on nalidixic acid
Nt_dilution	Dilution factor for Nt plates on non-selective agar
Nt_N0_ratio	Ratio of final to initial population size
Nt_SD	Standard deviation between the 3 estimates of Nt1,2 and 3
Nt_total	Nt_genotype plus Nt_coculture_strain
sd_m_coculture_strain	Calculated as in (98): $\frac{1.225\times m^{0.315}}{\sqrt[2]{N\_cultures}}$ for the coculture strain
sd_m_genotype	Calculated as in (98): $\frac{1.225\times m^{0.315}}{\sqrt[2]{N\_cultures}}$ for the focal strain
Sel_CFU1-19	Number of mutant colonies counted in each parallel culture.
Treatment	Concatenation of: genotype2, Oxygen, External_treatment, GlcMedia
Weight0	Initial weight of the deep-96 well plate in grams
Weight24	Final weight of the deep-96 well plate in grams
Abs_670_res	Mean of Abs_670_res1-4
Abs_670_res1-4	Measurements of absorbance at 670nm of resazurin, MG cultures at the end of the fluctuation assay growth. Used as an indicator of anaerobiosis.
Layout	Plate layout used (for anaerobic assays a parallel aerobic assay plate was carried out with an identical layout, aside from this all layouts are randomly generated and unique).
MutationFrequency	Mean of Sel-1-19 divided by Nt_genotype multiplied by $1x10^9$
Oxygen	Presence of oxygen (+ for aerobic; - for anaerobic)
Notes	Any notes, e.g. on contamination, for the given assay.
w_relative	Relative fitness of the focal strain to the coculture strain
Experimentor	Initials of the experimentor
N0_rep1-3	CFU counts on 3 N0 plates. (For some coculture repeats N0 was plated 3 times and a mean used rather than a single plating. This was done for more accurate relative fitness estimations in some cocultures.)
D_perc_gen	D_genotype divided by D_total multiplied by 100 to give a percentage

		of the final density made up by the focal strain
	N0_mean_of_3	Mean of N0_rep1-3
SupData2_Peroxide.csv	Well	Location of the sample in the 96 well plate
	Sample	Arbitrary identifier for the 3 repeats from a single sample+AUR reaction
	PriorAvg	Measurement of background fluorescence prior to HRP addition to the reaction averaged across the 3 replicates
	PostAvg	Measurement of fluorescence immediately after HRP addition to the reaction averaged across the 3 replicates
	Post2Avg	Measurement of fluorescence ~1 minute after HRP addition to the reaction averaged across the 3 replicates
	PriorRaw	Measurement of background fluorescence prior to HRP addition to the reaction for the individual well
	PostRaw	Measurement of fluorescence immediately after HRP addition to the reaction for the individual well
	Post2Raw	Measurement of fluorescence ~1 minute after HRP addition to the reaction for the individual well
	OD_bc	Optical density of the sample prior to filter sterilisation for H_2O_2 measurement
	time	Time in hours from the start of the cultures growth at which the samples were taken for measurement
	AddH2O2	Additional H_2O_2 in the standards from diluted 3% H_2O_2
	Strain	Identity of the bacterial strain used
	Glucose	Concentration of glucose in mg per L
	LB	Percentage of LB i.e. 2% would equate to 440µL in 22mL of davis minimal media
	Catalase	Units per mL of catalase added
	RepNum	Repeat number where the same treatment was included twice in the same experimental plate from independent cultures
	Week	Identifier for the start date of the experiment
	Block	Identifier for the experimental block

CellRemovalMethod	Method of cell removal (syringe is filtration through a 0.22µm PES filter)
GAIN	The set gain on the plate reader for fluorescence readings
Treatment	Concatenation of Strain, LB, Catalase, Glucose
NetAvg	PostAvg – PriorAvg
NetFU	PostRaw – PriorRaw
Repeat	Concatenation of Treatment, RepNum
Nutrient	Nutrient source (LB for lysogeny broth or Glc for glucose)

Table. S3: Descriptions for columns in supplementary data tables ***SupData2_Peroxide.csv and SupData1_FluctuationAssays.csv .***

Supplementary Files:

00_SupCode1.R: R code necessary to recreate ODE modelling (Fig. 1, 2, S1, S2, S14, S15)
00_SupCode2.R: R code necessary to recreate lab work analysis (Fig. 3, 4, S3, S4, S5, S6, S7, S8, S9, S10, S11, S12, S13)
SupplementaryStats.docx: Details of statistical models used in this study.
SupData1_FluctuationAssays.csv: Data from fluctuation assays needed to run 00_SupCode2.R
SupData2_Peroxide.csv: Data from amplex ultra-red peroxide assays needed to run 00_SupCode2.R
SupData3_Jain09.txt: Data available from (81) used to fit U1 parameter in 00_SupCode1.R
SupData4_Krasovec2017.txt: Data available from (3) used to fit Met1 parameter in 00_SupCode1.R